Politecnico
di Torino

Politecnico di Torino

MSc in Automotive Engineering

Determination of Hydrogen susceptibility of Internal Combustion engine components through permeation tests.

Candidate: Mudumbai Anirudh Badrinath

Supervisors: Paolo Matteis, Dr. Giorgia Ghiara

Academic Year 2026

Abstract

The ongoing transition from diesel to hydrogen as an automotive fuel raises critical questions regarding the susceptibility of aluminium engine components to hydrogen-induced degradation. This thesis presents the electrochemical investigation of hydrogen permeation behaviour across five aluminium alloy specimens. Three reference alloys – Al-Si-4015, Al-5083 and Al-6016 and two automotive engine components, an engine head (A319 cast alloy) and an inlet manifold (A380 cast alloy), used in a Hydrogen fueled internal cobustion engine.

Hydrogen permeation experiments were conducted using the Devanathan–Stachurski (DS) electrochemical cell in accordance with the frameworks established by ISO 17081 and ASTM G148. Specimens were prepared with platinum sputter coatings (30–50 nm) on the oxidation side to provide a stable, conductive and electrochemically active surface for hydrogen oxidation, minimizing the influence of the native aluminium oxide and ensuring reproducible hydrogen permeation measurements. All experiments were performed at room temperature (298 K) using 0.1 M KOH electrolyte in both compartments to avoid chloride-induced pitting corrosion of the aluminium surface.

Apparent diffusion coefficients were obtained from the permeation transients using both the time-lag $D_{\text{app}}^{\text{tl}} = \frac{L^2}{6\,t_{\text{lag}}}$ and the breakthrough time $D_{\text{app}}^{\text{bt}} = \frac{L^2}{15.3\,t_{\text{bt}}}$method. Trap binding energies used in the trapping analysis was selected based on literature values associated with relevant hydrogen trapping sites in aluminium alloys. It should be noted that the binding energy is a property of the interaction between hydrogen and a specific trapping site, rather than an intrinsic property of the alloy itself.[1][2][3] and trap densities were quantified using Oriani's local equilibrium trapping theory. Microstructural analysis was performed using optical microscopy and scanning electron microscopy (SEM). Second phase volume fractions were quantified via ImageJ image analysis and the Delesse stereological principle, enabling a interface trap density to be calculated from the image analysis data.

The results revealed that the three reference alloys all exhibited apparent diffusion coefficients below the accepted aluminium lattice diffusivity ($D_L = 1.88 \times 10^{-10}\,\text{m}^2\,\text{s}^{-1}$)[3], confirming physically valid trapping behaviour. Al-4015 displayed near-lattice diffusion ($D_{\text{app}} = 1.32 \times 10^{-10}\,\text{m}^2\,\text{s}^{-1}$) with a low trap density attributed to sparse Si-particle interfaces. Al-5083 exhibited moderate trapping ($D_{\text{app}} = 1.09 \times$

$10^{-10}\,\mathrm{m^2\,s^{-1}}$), with image analysis indicating that second phase interfaces account for only $\approx$ 18% of the measured trap density, implying significant contributions from Mg–vacancy complexes and grain boundaries. Al-6016 displayed the most retarded diffusion ($D_{\mathrm{app}} = 2.69 \times 10^{-11}\,\mathrm{m^2\,s^{-1}}$) and the highest trap density consistent with a dense network of Mg_2Si precipitate interfaces, grain boundaries, and dislocation substructures. In contrast, only one of the engine components, i.e., the inlet manifold, exhibited apparent diffusivities that exceeded the lattice value, while Oriani's trapping model was physically invalid for other the specimen showing that the apparent diffusivity was lower than the lattice diffusivity of aluminium. EDS mapping, the rapid permeation transient and the cast microstructure gives us the idea that the intermetallic phases facilitate rapid hydrogen transport rather than classical bulk lattice diffusion for the cast automotive alloys particularly the A319 (Engine Head). These findings establish a clear ranking of hydrogen susceptibility across the alloy families and demonstrate that automotive cast engine components operate in a fundamentally different manner relative to their wrought counterparts. The results provide quantitative data and microstructural insight to support alloy selection, component design, and mitigation strategies for hydrogen embrittlement risk in aluminium systems used in next-generation hydrogen-fueled automotive engines.

Acknowledgements

I would like to thank the faculty and staff of DISAT (Department of Applied Science and Technology) at Politecnico di Torino for providing the resources and academic environment necessary for the successful completion of this project.

My heartfelt appreciation goes to my colleagues and friends for their support and encouragement during the various stages of this research. I would also like to express my sincere gratitude to my partner Rutuja Patil for her unwavering support, encouragement and understanding throughout the completion of this thesis.

Finally, I am deeply grateful to my family for their support, understanding and motivation throughout my academic journey. Their constant encouragement has been my source of strength and inspiration.

This thesis would not have been possible without the contributions and support of all those mentioned above.

Thank you.

Contents

Chapter 1

Introduction

Hydrogen embrittlement (HE), also known as Hydrogen Induced Cracking, is a phenomenon that degrades the ductility, toughness, and strength of metallic components through the interaction of hydrogen with a material's microstructure. Due to their small atomic size, hydrogen atoms permeate through the crystal lattice, leading to sudden and premature failure under stress. HE is most commonly associated with pipeline steels, storage tanks, and alloys of nickel, cobalt, and titanium whereas materials such as copper and aluminium are considered comparatively less susceptible. However, recent investigations from Zhao et. al.[4] and Safyari et. al.[5] have demonstrated that high-strength aluminium alloys can exhibit significant embrittlement under specific conditions, including exposure to moisture, water vapour, and microstructural features such as semi-coherent precipitates that saturate with hydrogen, despite aluminium's inherently low hydrogen solubility and protective passive oxide layer.

Zhao et al.[4] investigated the susceptibility of high-strength aluminium alloys to hydrogen embrittlement, noting that while these alloys offer significant lightweighting potential for vehicles, the exact mechanisms underpinning hydrogen-induced failure remain poorly understood due to the difficulty of atomic-scale hydrogen analysis. Through near-atomic-scale characterisation of a 7xxx Al alloy, the authors revealed that hydrogen co-segregation at grain boundaries promotes decohesion, while partitioning of hydrogen into second-phase particles can inhibit embrittlement — offering a key microstructural design strategy.

Chen et al.[6] reviewed hydrogen embrittlement in aluminium alloys used for vehicle-mounted high-pressure hydrogen storage tanks, emphasising that susceptibility to hydrogen-induced degradation under high-pressure conditions poses considerable safety risks to vehicles and passengers. The review comprehensively covers HE formation mechanisms including **HELP** (Hydrogen Enhanced Localized Plasticity) and **HEDE** (Hydrogen Enhanced De-cohesion) alongside detection and prevention methods, making it a directly relevant reference for aluminium alloy performance in automotive hydrogen applications.

Although substantial research has been conducted on hydrogen transport and embrittlement in high-strength aluminium alloys and hydrogen storage applications, comparatively little work has focused on hydrogen permeation behaviour in aluminium alloys used directly in hydrogen-fuelled internal combustion engine components. Recent investigations into hydrogen-fuelled engine materials have highlighted the need for a better understanding of hydrogen interaction with cast and wrought aluminium alloys under service-relevant conditions. The present work addresses this gap by comparing hydrogen permeation behaviour, trapping characteristics, and microstructural influences across representative Al–Si, Al–Mg, and Al–Mg–Si alloys as well as two commercially used automotive engine components[7].

In particular, this thesis examines the effects of HE in automotive engine components fabricated from three wrought alloys Al–Si (4015), Al–Mg (5083), and Al–Mg–Si (6016) alloys and two cast aluminium alloys, namely, A319 (Engine Head) and A380 (Inlet Manifold) used for components in a hydrogen fueled combustion engine. This addresses a gap in the literature whereby the specific implications of transitioning from diesel to hydrogen as an automotive fuel and the consequent increase in hydrogen permeation in engine components have yet to be systematically compared.

Chapter 2

State of the Art

This section of the thesis reviews the current state of knowledge on the measurement of hydrogen translport and trapping in metals by means of the D-S cell, with particular reference to aluinium alloys drawing on experimental studies and literature to establish the foundation upon which this thesis is built.

2.1 The Devanathan-Stachurski cell

Devanathan and Stachurski[8] introduced the electrochemical hydrogen permeation technique that forms the basis of modern studies on hydrogen transport in metals. In their work, a thin palladium membrane was mounted between two electrochemical compartments. Hydrogen was generated cathodically on one side of the membrane, adsorbed onto the metal surface, and absorbed into the palladium lattice as atomic hydrogen. The absorbed hydrogen then diffused through the membrane under the concentration gradient established between the charging and oxidation sides. On the opposite side, the diffusing hydrogen was anodically oxidized back to protons, producing an electrical current directly proportional to the hydrogen flux through the membrane. By recording the transient increase in oxidation current from the onset of charging to steady-state conditions, the authors demonstrated that hydrogen transport obeys Fick's laws of diffusion and showed that the diffusion coefficient could be calculated from the same transient. This study provided the first electrochemical method for determining hydrogen diffusivity in metals and established the conceptual framework for subsequent measurements of hydrogen solubility, trapping, and permeation in metals. The two-compartment Devanathan–Stachurski cell introduced in this work remains the standard experimental configuration and serves as the foundation for internationally recognized methodologies such as ISO 17081 and ASTM G148[9].

In electrochemical hydrogen permeation experiments, the condition of the oxidation (exit) surface is critical because the measured anodic current is only proportional to the hydrogen flux if every hydrogen atom arriving at that surface is immediately

oxidized to protons. In practice, bare iron surfaces rapidly form oxide and hydroxide films, especially in alkaline electrolytes such as 0.1 M NaOH, and these passive layers introduce an additional kinetic resistance that can slow hydrogen oxidation and cause an underestimation of the true permeation flux. To eliminate this limitation, Zafra et al.[10] deposited a thin palladium coating of approximately 50 nm on the oxidation side of the cold-rolled iron membrane by electroplating before each experiment. Palladium was selected because it has exceptional catalytic activity for hydrogen oxidation as it facilitates hydrogen oxidation and promoters hydrogen entry or transmission through the surface, ensuring that hydrogen atoms emerging from the iron are rapidly converted into an electrical current. The coating serves two principal purposes: first, it accelerates the electrochemical reaction kinetics so that the oxidation step is no longer rate-limiting; second, it protects the iron substrate from direct contact with the alkaline solution, thereby minimizing oxide formation and preventing surface passivation during prolonged testing. By maintaining a highly active and stable oxidation surface, the palladium layer ensures that the measured current accurately reflects hydrogen diffusion through the bulk material rather than artifacts associated with surface chemistry. This treatment is particularly important at elevated temperatures, where oxidation and surface instability become more pronounced. The use of palladium coatings is therefore a standard practice in Devanathan–Stachurski permeation experiments and is essential for obtaining reproducible breakthrough times, lag times, and steady-state currents from which reliable diffusion coefficients can be calculated.

The standard method to determine the diffusivity, by using the D-S cell, is as follows: [8][9] Hydrogen transport is governed by Fick's second law 2.1:

$$\frac{\partial C}{\partial t} = D_{\text{app}} \frac{\partial^2 C}{\partial x^2} \tag{2.1}$$

The analytical solution, expressed as normal flux ratio, is given by Fourier Series 2.2:

$$\frac{J(t)}{J_{ss}} = 1 + 2\sum_{n=1}^{N} (-1)^n \exp\left(-n^2 \pi^2 \tau\right) \tag{2.2}$$

where

$$\tau = \frac{D_{\text{app}}\, t}{L^2}$$

is the dimensionless Fourier time.

D_{app} can therefore be extracted from selected points of the hydrogen transport transient in eq. 2.2[9]

Two methods are commonly used[5].

In the Time-Lag method, the lag time t_{lag} is identified as the time at which the normalized flux reaches 63% of its steady state value. The apparent diffusivity is

calculated as:

$$D_{\text{app}}^{\text{tl}} = \frac{L^2}{6\, t_{\text{lag}}} \tag{2.3}$$

In the Breakthrough time method, the breakthrough time t_{bt} corresponds to the point where the flux reaches 10% of the steady state value and the apparent diffusivity is calculated as:

$$D_{\text{app}}^{\text{bt}} = \frac{L^2}{15.3\, t_{\text{bt}}} \tag{2.4}$$

The constants 6 and 15.3 are derived analytically from the Fourier series solution in eq. 2.2 evaluated at their respective normalized flux thresholds.

Danielson[11] describes the use of the Devanathan-Stachurski (DS) electrochemical cell. Although the DS cell was used widely for steels and other metals, applying it to aluminium was difficult because aluminium rapidly forms a passive oxide layer which blocks hydrogen transport, causes unstable electrochemical behaviour and promotes localized corrosion (especially pitting). He demonstrated that the Devanathan–Stachurski technique can be adapted for aluminium alloys by using sputtered palladium coatings and chromate-containing electrolytes to suppress pitting. Diffusion coefficients of $3.3 \times 10^{-10}\,\text{m}^2\,\text{s}^{-1}$ for AA5083 and $1.6 \times 10^{-10}\,\text{m}^2\,\text{s}^{-1}$ for AA6061 were reported, and the study showed that both anodic and cathodic polarization enhance hydrogen entry, while oxide-film properties dominate permeation behaviour.

2.2 Hydrogen Trapping

Oriani[12] developed the thermodynamic framework that remains the cornerstone for interpreting hydrogen permeation and trapping experiments in metals. In his work, hydrogen was considered to occupy two distinct populations of sites within the metal: normal interstitial lattice sites, through which hydrogen is mobile and contributes directly to diffusion, and reversible trap sites associated with microstructural defects such as dislocations, grain boundaries, vacancies, secondary phase particles, and phase interfaces. The central assumption of the model is that hydrogen exchanges rapidly between these two populations, so that local thermodynamic equilibrium is maintained throughout the specimen during diffusion. Under this assumption, the relative occupancy of lattice and trap sites is governed by an equilibrium constant (K) following an exponential law,

$$K = \exp(E_b/RT) \tag{2.5}$$

where E_b is the trap binding energy. R is the Universal gas constant with a value of 8.314 J/molK and T is the temperature. Oriani showed that the experimentally measured diffusion coefficient is therefore not the true lattice diffusivity, but an apparent diffusivity D_{app} reduced by the presence of traps according to eq.2.6

$$D_{\text{app}} = D_L \div (1 + \frac{KN_T}{N_L}) \tag{2.6}$$

where D_L is the lattice diffusion coefficient, N_T is the trap density, and N_L is the density of interstitial or lattice sites. This relationship demonstrated quantitatively that increasing trap density or increasing trap binding energy can reduce the apparent diffusion coefficient by several orders of magnitude, substantially lengthen lag times and breakthrough times in Devanathan–Stachurski permeation experiments, and can increase the total hydrogen inventory within the metal, without necessarily changing the fundamental lattice transport properties. By comparing the model with experimental data for steels with different carbon contents, heat treatments, and degrees of cold work, Oriani showed that dislocations introduced by plastic deformation and interfaces associated with carbides act as significant reversible trapping sites, with binding energies typically in the range of approximately 17–46 kJ/mol [13] . Young and Scully[14][3] reported reversible hydrogen trapping associated with defects such as dislocations in aluminium, with binding energies in the range of approximately 0.28 eV. Calculations by Yamaguchi et al.[15] demonstrated that Fe–Cu-containing Al_7FeCu_2intermetallic compounds can exhibit hydrogen trapping energies of up to approximately 0.56 eV/H. These literature values were therefore used as a basis for selecting representative binding energies according to the microstructural characteristics of the investigated alloys. The theory explained why cold-worked and higher-strength steels exhibit lower apparent diffusivities and greater hydrogen retention, and helped to increase their increased susceptibility to hydrogen embrittlement. More broadly, the study established the critical distinction between lattice diffusivity and effective diffusivity, provided a rigorous means of estimating trap density and binding energy from electrochemical permeation transients, and demonstrated that much of the variability in experimentally reported diffusion coefficients arises from differences in microstructure rather than differences in intrinsic hydrogen mobility.

2.3 Oxidation and Pitting

Aluminium is naturally protected by a thin, compact oxide film composed primarily of Al_2O_3 and hydrated aluminium hydroxides, which forms spontaneously within milliseconds upon exposure to air or water [16]. This passive layer is highly adherent and normally prevents further corrosion, making aluminium one of the most corrosion-resistant structural metals. However, in chloride-containing solutions such as NaCl, chloride ions are specifically adsorbed onto defects in the oxide film and migrate through the passive layer to the metal/oxide interface, where they disrupt the oxide structure and promote localized dissolution. Natishan and O'Grady[17] and Frankel (1998) [18] demonstrated

that chloride becomes incorporated into the oxide and weakens its protective properties, ultimately leading to breakdown of the passive film and initiation of pitting corrosion. Once a pit forms, the local environment becomes enriched in chloride ions and increasingly acidic, which accelerates dissolution and leads to hydrolysis of Al^{3+} ions. The acidification of the environment is related to the formation of $Al(OH)_3$ and then Al_2O_3 through the uptake of the OH^- from the solution. Parallelly, Cl^- ions remain on the pit surface and electrostatically attracts the H^+ ions which in turn create local acidification that does not allow the formation of the passive film in a self sustaining system. Szklarska-Smialowska (1999)[19] established that pitting corrosion of aluminium occurs when chloride ions locally break down the passive oxide film, initiating metastable pits that can develop into stable pits once a critical electrochemical condition is reached. Within these pits, hydrolysis of dissolved aluminium ions lowers the pH and concentrates chloride ions, creating an autocatalytic environment that sustains rapid localized dissolution and promotes hydrogen evolution. Natishan and O'Grady (2014)[17] complemented this work by demonstrating through XPS and SIMS that chloride ions are incorporated directly into the passive oxide and accumulate near the metal/oxide interface, thereby weakening the film at the atomic scale. Together, these studies show that NaCl solutions induce highly localized corrosion and non-uniform hydrogen charging in aluminium, whereas chloride-free alkaline electrolytes such as KOH avoid passive film breakdown and provide more homogeneous and reproducible conditions for electrochemical hydrogen permeation experiments. In electrochemical permeation experiments, this localized attack produces non-uniform hydrogen charging, changes the effective surface area, and introduces substantial scatter into the measured breakthrough and lag times. For this reason, chloride electrolytes are generally unsuitable for aluminium permeation studies. Instead, alkaline solutions such as KOH are commonly used because they do not contain aggressive chloride ions. Although aluminium is amphoteric and can dissolve in strong alkali, this dissolution occurs more uniformly over the surface rather than through stochastic pit formation. As a result, KOH provides a more stable and reproducible electrochemical environment, allowing hydrogen to be introduced more homogeneously across the membrane and enabling more reliable determination of diffusion coefficients.

Chapter 3

Material and Methods

For the materials, we chose commercially used aluminium alloys from the Al-Si (4015), Al-Mg (5083), and Al-Mg-Si (6016) series, reflecting the alloy families most employed in the fabrication of automotive engine components.

3.1 Examined Materials:

Reference materials

a. 4015 Al Alloy sheet (1.27 mm thickness):

4015 (Al-Si)[20] is a wrought alloy with good ductility and mechanical strength. It was formed as a general purpose alloy. Due to its high silicon content, this alloy can be anodized, welded or painted. Cold workability, gas weldability, arc weldability , solderability, and brazability of the alloy is excellent.[21][22]

b. 5083 Al Alloy sheet (1.40 mm thickness):

5083 series aluminium alloys are aluminium-magnesium (Al-Mg) alloys (0.5%-5.5% Mg) known for excellent corrosion resistance, particularly in marine environments, high strength without heat treatment, and superior weldability. These non-heat-treatable, strain-hardenable alloys are strong, ductile, and maintain high toughness at cryogenic temperatures, making them ideal for shipbuilding, pressure vessels, and structural applications[21][22].

c. 6016 Al Alloy sheet (1.05 mm thickness):

6016 series aluminium alloys (Al-Mg-Si) are versatile, heat-treatable, wrought alloys known for excellent extrudability, moderate-to-high strength (200 - 350 MPa), and superior corrosion resistance. They are primarily used in structural, automotive, and

architectural applications (e.g., frames) due to good weldability, formability, and surface finishing (anodizing)[21][22]

Engine materials

a. Engine Head - A319 casting alloy:

The engine head (cylinder head) serves as the structural cap to the combustion chamber while housing important parts such as the inlet and exhaust ports, valve seats and spark plug housing.

b. Inlet Manifold - A380 casting alloy:

The inlet manifold is a critical component responsible for distributing the air-fuel mixture evenly across all cylinders.

3.2 Chemical analysis - Optical Emission Spectroscopy

The chemical composition of the three aluminium alloy samples investigated in this study was determined by optical emission spectroscopy (OES), commonly referred to as spark analysis.

Spark Optical Emission Spectroscopy (OES) is a technique used to determine the chemical composition of metal alloys by exciting atoms with an electrical spark. The resulting excited atoms emit characteristic light wavelengths, which are measured to quantify the precise amount of each element.

Using this technique the alloys are characterized with their constituent elements with accurate readings.

3.3 Sample Preparation:

Pristine samples of the alloy (Al-4015, Al-5083 and Al-6016) specimen were cut with a precision abrasive cut saw 3.1a and hot-embedded in Bakelite resin powder with the LECO PR-63 Mounting Press 3.1b at 180°C for 9 minutes until the resin hardened and it was then taken out. We also prepared cold embedded samples with acrylic resin left overnight to harden to observe the difference in hot and cold embedding influencing the alloy's Platinum coating.

The embedded samples were ground on a rolling polish machine 3.2 using silicon carbide (SiC) abrasive papers of 600, 1200 and 2500 grit in sequence, followed by a final polishing with 3 µm and 1 µm diamond suspensions to obtain a smooth, mirror-like surface for microstructural analysis. The samples to be used for permeation went

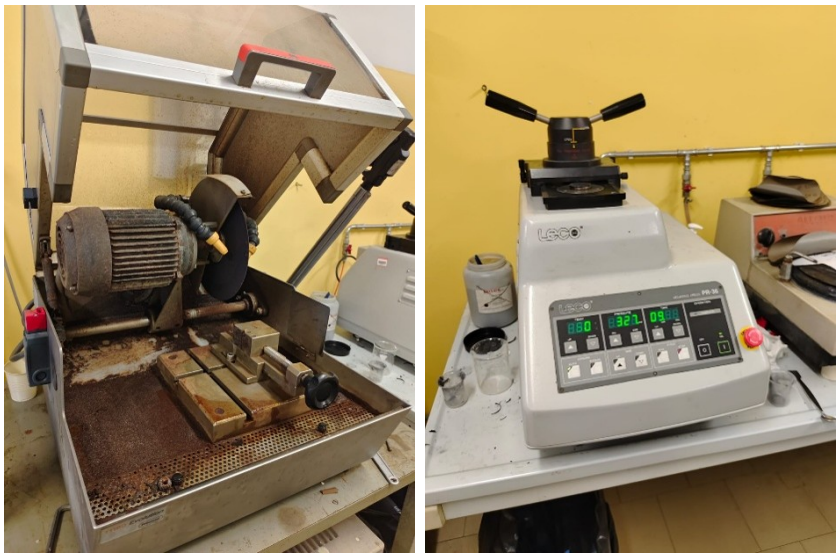

Figure 3.1: a) Precision abrasive cut saw. b) LECO PR-63 Mounting press for embedding.

through the same procedure wherein the side facing the anodic compartment in the DS cell would be polished with a 2500 grit silicon carbide (SiC) abrasive paper and the side facing the cathode would be polished with 3 µm and 1 µm diamond suspensions to obtain a mirror finish. The mirror-polished charging surface minimizes the influence of surface roughness on hydrogen absorption and promotes uniform hydrogen entry into the material, while the 2500-grit finish on the oxidation side provides an adequate surface for hydrogen oxidation without affecting the measured permeation response. The use of different surface finishes on the two sides of the specimen was based on preliminary investigations performed in previous work, which demonstrated that polishing the oxidation side to a mirror finish did not produce a measurable difference in the hydrogen permeation transients or in the calculated diffusion parameters. Consequently, the adopted preparation protocol reduces specimen preparation time while maintaining the reliability and reproducibility of the permeation measurements.

Figure 3.2: Rolling polish machine

After each polish the surface of the samples were rinsed with distilled water and then ethanol to remove any water residue and then blow-dried until the ethanol has completely evaporated. After the permeation experiment is complete the cross section of the sample is cut and undergoes the above-mentioned metallographic procedures along with an ultrasonic bath to remove any embedding or polishing residue that might remain on the surface to be analyzed under Optical microscope or SEM.

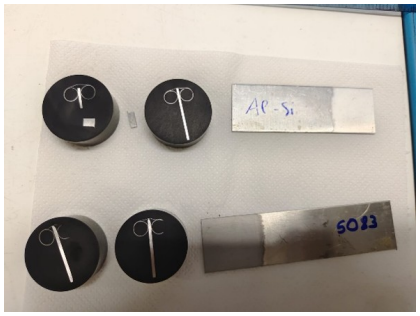

Figure 3.3: Embedded samples of Al-4015 and Al-5083

Pre-coating of the specimens:

Palladium Coating – Palladium was electrochemically plated on the surface of the samples following the precedure described by[23]. The used solution contained 3.5% (w/w) NaCl, 0.01 M KNO_2 and 0.001 M $PdCl_2$. In a 1 L flask 35 g of NaCl, 0.8511 g of KNO_2, 0.17733 g of $PdCl_2$ were added. Before placing the specimen in the solution, the face was pre-polished to electroplate with 0.5 M KOH. The surface of the sample was then cleaned with a cotton swab soaked in the 0.5 M KOH solution until a bright surface was obtained. Samples were then cleaned dry with a fresh cotton swab and rinsed in

situ with ethanol before the immersion. The palladium was electrodeposited galvanostatically for 20 minutes using a current generator (TT EL301R). During deposition, the cell was purged with N_2 gas to further prevent oxidation of the aluminium surface. Plating was commenced with 1.0 mA/cm^2 for 15 minutes, followed by 10 mA/cm^2 for an additional 5 minutes following the described procedure [23]. The voltage increased slightly from 688 to 697 mV, indicating stable electrochemical conditions.

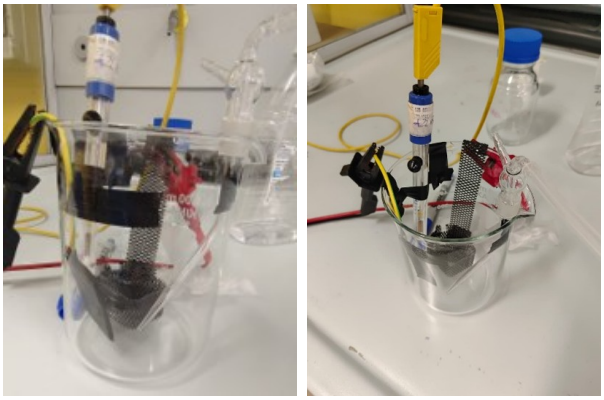

Figure 3.4: Electrolytic cell to electrochemically plate Pd over specimen surface.

Platinum Coating – The alloy surface was sputter coated with Platinum initially with 5 nm using a Quorum Q150T ES sputter coater. After subsequent tests we coated 30 nm and 50 nm to optimize the protocol. Platinum sputter coating was applied to all three alloy samples as a replacement for the electrochemically plated palladium coating, which was found to produce an uneven surface deposition unsuitable for the hydrogen permeation experiment[10]. The uniform and adherent coating achieved through platinum sputtering ensured a consistent surface coverage across all samples, which is critical for obtaining reliable and reproducible hydrogen permeation measurements.

Figure 3.5: Quorum Q150T ES sputter coater

3.4 Permeation tests

In this section two different methodologies were chosen for permeation tests. Preliminary testing revealed that the original methodology promoted localized corrosion of the aluminium specimens, which affected the integrity of the catalytic coating and influenced the hydrogen permeation response. Consequently, the electrolyte composition and surface preparation protocol were revised to establish a more stable electrochemical environment while maintaining the fundamental operating principles of the Devanathan–Stachurski (DS) cell. Both methodologies adopted for the permeation experiments are described below.

First Methodology –
The cell is composed of two compartments (oxidation and reduction) separated by the metal sample which serves as the working electrode (WE). The oxidation cell was configured as a three-electrode system comprising the specimen as the working electrode (WE), an Ag/AgCl reference electrode (RE, E = 0.197 V vs Ag/AgCl) for potential control, and a platinum tipped counter electrode (CE) to complete the electrical circuit. The reduction cell is comprised of the alloy as the Working Electrode (WE) and a counter electrode (CE) which was a Titanium mixed metal oxide (TiMMO©) electrode. The anodic side was polarized anodically to generate hydrogen. The anodic side was also filled with 3.5% of NaCl while the cathodic side was filled with 0.01 M KOH. The anodic compartment was also purged with N_2 gas as a precaution for the aluminium to not oxidize.

Al-5083: The first specimen on which the Permeation experiment was carried out was the Al-5083 alloy coated with a thin layer of Palladium. The thickness of the specimen was 1.4mm. After checking for the Open Circuit potential(OCP), it was observed to be at -0.850 V. A potentiostatic scan was imposed through the GAMRY Potentiostat (Reference 620) and the current density was measured. The Working Electrode was conditioned to reach a current density lower than 900 $\mu A/cm^2$. The decrease in current density is measured to have a better resolution of the curve. Once the current density was below 1 mA/cm^2, the KOH was added into the cathodic chamber and a galvanostatic current was imposed in the cathodic compartment to observe the rise in current as an indicator that the permeation has occurred.

Al-6016: The second specimen was the Al-6016 series pre-coated with a thin layer of Palladium. The thickness of the sample was 1.03-1.04mm. We keep the same conditions as the pervious alloy and the OCP was observed to be -1.108 V. Keeping all the conditions and procedures constant we observed for the change in current.

Figure 3.6: Palladium coated region on Al-6016 sample.

Second Methodology –

The second methodology of electrochemical permeation was carried out with the same conditions as the first methodology but instead of 3.5% of NaCl, 0.1 M KOH was used in the anodic and cathodic chambers of the DS cell. his modification was introduced after preliminary permeation experiments revealed significant pitting corrosion on the surface of the aluminium specimens, particularly for the Pd-coated Al-6016 and Pt-coated Al-4015 alloys. The localized corrosion compromised the integrity of the catalytic coating and could potentially affect the reproducibility and accuracy of the hydrogen permeation measurements. The KOH was used as the electrolyte for both the anodic and cathodic compartments to establish a more stable alkaline environment, minimize chloride-induced corrosion, and obtain more controlled and reproducible hydrogen permeation measurements. In addition, Platinum was used instead of Palladium as the palladium was not coated evenly over the surface and as such, we encountered difficulties with permeation. The purging of N_2 gas was stopped as the Platinum coating was well distributed on the surface of the specimen.

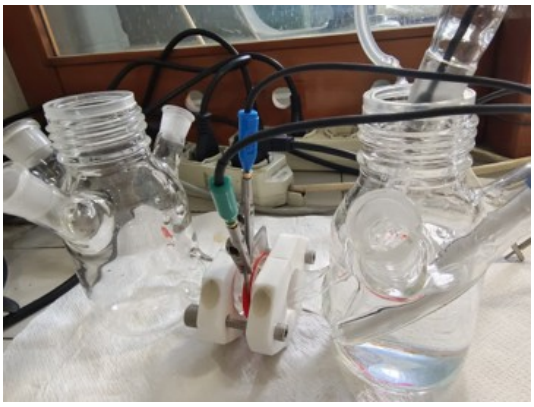

Figure 3.7: Permeation Cell showing the Working electrode (Alloy sample) in between the Anodic compartment (Right) and the cathodic compartment (Left).

Al-4015: We sputter coated the aluminium specimen with 30 nm of Platinum. We

switch the electrolytes in the anodic and cathodic compartment to 0.1 M KOH as the NaCl electrolyte induced corrosion very rapidly. The thickness of the specimen was 1.25-1.26 mm. We run a Potentiostatic scan through the anodic compartment until the current dropped to 960 µA/cm^2 to condition the surface of the Working Electrode (WE) before pouring the KOH into the cathodic compartment and a galvanostatic scan was passed through the cathodic compartment.

Al-5083: We sputter coated the aluminium specimen with 30nm of Platinum. The thickness of the specimen was 1.25-1.26 mm. We run a Potentiostatic scan through the anodic compartment until the current dropped to 379 µA/cm^2 to condition the surface of the Working Electrode (WE) before pouring the KOH into the cathodic compartment and a galvanostatic scan was passed through the cathodic compartment.

Al-6016: For this alloy we decided to test the integrity of the platinum coating. We started with 6 nm of platinum coating and performed the experiment as the same. The thickness of the sample was 1.03-1.04 mm. After the initial experimental trials, the coating thickness was increased to 50 nm for the remaining permeation experiments. The implications of the coating thickness on the experimental behaviour are discussed in the Results section. After increasing the thickness of the coating, the experiment was carried out with keeping the same conditions as before. The current dropped close to 600 µA/cm^2, conditioning the surface of the Working Electrode before pouring the KOH solution into the cathodic chamber and a galvanostatic scan was passed through the cathodic compartment.

Engine Head: We performed the same procedures, and the specimen was coated with 50 nm of Platinum. The thickness was found to be 0.65-0.67 mm. The KOH electrolyte was poured into the cathodic chamber when the current dropped to 389 µA/cm^2 and we observed for permeation.

Inlet Manifold: As with the previous alloys, the procedure for this specimen is no different. The thickness of the specimen was 0.30-0.50 mm, the thinnest specimen of all. After placing the specimen in between the cell, a potentiostatic scan was passed through the anodic compartment to condition the surface of the Working Electrode (WE) until the current dropped to 340 µA/cm^2. When adding the electrolyte in the cathodic compartment and passing a galvanostatic scan through the cathodic chamber we observed for the rise in current indicating permeation.

3.5 Analysis of permeation curves

The calculation of the permeation curves were done on MATLAB using the literature presented by Fick's Second Law and Fourier series solution[8][9], Apparent diffusion coefficient [9] and Oriani's trapping theory[12].

The experimentally measured oxidation current at the anodic (exit) side of the specimen is first converted into hydrogen flux using Faraday's law:

$$J(t) = \frac{I(t) - I_0}{FS} \tag{3.1}$$

where I(t) is the measured current, I_0 is the background current, F is Faraday's constant (96500 As/mol) and S is the exposed specimen area (0.000239 m^2). The resulting flux transient is smoothened to reduce experimental noise and normalized with respect to the steady-state flux J_∞.

Prior to diffusivity analysis, the experimental hydrogen flux data was smoothened using a moving-average filter with a window size of 30 data points $\text{smoothdata}('\text{movmean}', 30)$

The moving-average method replaces each data point with the mean value of its neighbouring points, thereby reducing random fluctuations and noise in the permeation signal. This results in more reliable calculations of the apparent diffusivity and trapping parameters.

From the normalized permeation curve, the Breakthrough time (t_{bt}) corresponding to $0.1\times J_\infty$ and Lag time (t_{lag}) corresponding to $0.63\times J_\infty$ are determined. These characteristic times are used to calculate the apparent hydrogen diffusivity according to the Breakthrough time and Lag time methods:

$$D_{app}^{bt} = \frac{L^2}{15.3 t_{bt}} \tag{3.2}$$

$$D_{app}^{tl} = \frac{L^2}{6 t_{lag}} \tag{3.3}$$

where L is the specimen thickness.

By using Oriani's theory, if the lattice diffusivities and the trap binding energy are known or can be estimated, the trap density can be calculated by rearranging equation 2.5 and 2.6 as follows:

$$N_T = N_L \left(\frac{D_L}{D_{\text{app}}^{\text{tl}}} - 1 \right) \exp\left(-\frac{E_b}{RT} \right) \tag{3.4}$$

where D_L is the lattice diffusivity of hydrogen in aluminium which was calculated from pure aluminium at room temperature[3], D_{app}^{tl} is the experimentally determined apparent diffusivity, E_b is the trap binding energy which is specific for each aluminium alloy, R is the universal gas constant and T is the absolute temperature.

To evaluate the influence of hydrogen trapping, the density of interstitial lattice sites (N_L) in aluminium is first calculated using the FCC lattice parameter a:

$$N_L = \frac{4}{a^3} = 6.025 \times 10^{28} \tag{3.5}$$

Finally, the molar trap concentration was obtained as:

$$C_T = \frac{N_T}{N_A} \tag{3.6}$$

where N_A is Avogadro's constant.

The trap Binding energies have been taken according to [14][15][3] as reference values for specific traps and vacancies within the alloys in table 3.1:

Table 3.1: Trap binding energies of Aluminium alloys.

Alloy	$\boldsymbol{E_b}$ **(eV)**
Al-4015	0.35
Al-5083	1.00
Al-6016	2.07
A319 (Engine Head)	0.35
A380 (Inlet Manifold)	0.55

Binding energy is converted from eV to J/mol:

$$E_b\,(\mathrm{J\,mol^{-1}}) = E_b\,(\mathrm{eV}) \times 1.602 \times 10^{-19} \times N_A \tag{3.7}$$

Theoretical permeation transients are calculated using the analytical solution of Fick's second law:

$$\frac{J(t)}{J_\infty} = 1 + 2\sum_{n=1}^{\infty}(-1)^n \exp(-n^2\pi^2\tau) \tag{3.8}$$

where

$$\tau = \frac{D_{app}t}{L^2} \tag{3.9}$$

is the dimensionless Fourier time. This solution was evaluated with N = 41 terms.

This theoretical permeation curve is compared with the experimental permeation curve. This comparison allows the calculated diffusivities and trapping parameters to be assessed by evaluating how accurately the theoretical response reproduces the measured hydrogen permeation behaviour.

3.6 Optical Microscope

Microstructural observations

Optical microscopy (LOM) was performed both before and after the hydrogen permeation experiments to evaluate the surface condition of the specimens and identify any microstructural or morphological changes induced during testing. Prior to the experiments, optical observations were used to verify the quality and uniformity of the surface preparation, ensuring the absence of scratches, defects, or polishing artefacts that could influence hydrogen entry and the uniformity of the palladium/platinum coating. Following the permeation tests, the specimens were re-examined to assess the occurrence of localized corrosion, pitting, coating degradation, or other surface damage resulting from the electrochemical exposure. These observations provided a rapid, non-destructive means of evaluating specimen integrity and complementing the electrochemical permeation results. Observations were made using a MEF3 optical microscope. The samples were observed under optical microscope to investigate aluminium alloys prior to SEM/EDS analysis. Observation was done for both the cross section and the specimen surfaces. The identification features mainly we looked for was the Palladium/Platinum coating on the surface of the specimen by observing the cross-section images and impurities which could be identified as precipitates present in the matrix of the alloy. The pristine samples of the 4015, 5083 and 6016 alloys were observed and were compared to the same alloys after permeation.

Calculation of volume fraction of the precipitates

The specimen's cross section was observed under the microscope, and possible precipitates were identified and analysed and processed using Image Analysis software ImageJ. We then determined the volume fraction of the of second-phase precipitates.

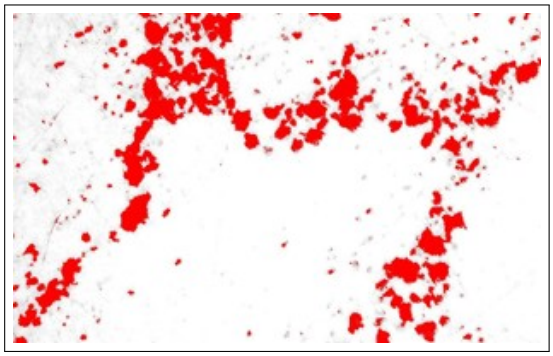

Figure 3.8: Image J red scale threshold on precipitates of A319 (Engine Head) sample.

The volume fraction of the precipitates was estimated using the Delesse stereological principle[24] which states that for a statistically representative planar section through

a microstructure:

$$V_f = A_f = \frac{A_{\text{precipitate}}}{A_{\text{total}}} \times 100\% \tag{3.10}$$

Where:

- V_f = volume fraction of precipitation phase
- A_f = area fraction of precipitates in the 2D micrograph
- $A_{\text{precipitate}}$ = total pixel area identified as precipitates
- A_{total} = total image area analysed

Slice	Count	Total Area	Average Size	% Area	Mean
Al-EH-precipitate-analysis.jpg	396	1743.257	4.402	12.150	198.772

Table 3.2: Average size and Area% (Volume fraction) of the A319 (Engine Head) sample

Image processing procedure:

Step 1 – Micrographs were imported into ImageJ, and scale was converted from pixel to micrometres.

Step 2 – The colour images were converted to 8-bit greyscale to enable thresholding based on intensity contrast between matrix and precipitates phases.

Step 3 – A red scale threshold was manually applied to segment precipitate pixels from the matrix.

Step 4 – The area fraction was extracted by obtaining the percentage of threshold pixels relative to the total region of interest (Table 3.2).

Step 5 – The procedure was repeated across a minimum of 10 representative fields. The mean volume fraction is given by:

$$\bar{V_f} = \frac{1}{n} \sum_{i=1}^{n} V_{f,i} \tag{3.11}$$

We first calculate mean precipitate radius by:

$$r = \sqrt{\frac{\overline{A}_{\text{precipitate}}}{\pi}} \tag{3.12}$$

The diameter would then be:

$$d = 2 \times r \tag{3.13}$$

We then calculated the interfacial area per unit volume by:

$$S_V = \frac{6V_f}{d} \times 10^6 \tag{3.14}$$

The result we are looking for is the Geometric trap density $N_T{}^{geo}$ as this value give us an independent, physically ground estimate of how many hydrogen trap sites exist in the material, derived from what we can see in the microstructure.

$$N_T^{\text{geo}} = S_V \rho_{\text{trap}} \tag{3.15}$$

Where: ρ_{trap} is the trap sites per unit interfacial area. It was estimated using the crystallographic planar atomic density[25] of the FCC aluminium 111 plane, the closest-packed plane and the common habit plane for coherent/semi-coherent precipitate-matrix interfaces in aluminium alloys. Using lattice parameter of a=0.405 nm the planar atomic density is:

$$\sigma_{(111)} = \frac{4}{\sqrt{3}\, a^2} = 14.079 \text{ atoms}\,\text{nm}^{-2} = 1.4 \times 10^{19} \text{ atoms}\,\text{m}^{-2} \tag{3.16}$$

We assume ρ_{trap} as $1 \times 10^{18}\,\text{m}^{-2}$ corresponding to an approximate atomic trap of 1 nm along the precipitate-matrix interface. This value corresponds to approximately one effective hydrogen trapping site for every fourteen interfacial atomic sites, based on a typical atomic surface density of 10^{19}m^2. The assumption reflects the fact that only a fraction of interfacial atoms provide favourable trapping sites for hydrogen. The adopted value is therefore used as an order-of-magnitude estimate to convert the measured interfacial area per unit volume into a geometric trap density[13].

Therefore for 1 in every 14 interfacial atomic sites:

$$\frac{1 \times 10^{18}}{1.4 \times 10^{19}} = 7\% \tag{3.17}$$

it represents approximately 7% of the total available interfacial atomic sites acting as effective hydrogen traps.

3.7 Scanning Electron Microscope (SEM)

Following the hydrogen permeation experiments, the specimens were examined using scanning electron microscopy (SEM) to characterize surface morphology and identify microstructural features associated with hydrogen charging and electrochemical expo-

sure. SEM employs a focused beam of high-energy electrons that scans the specimen surface, producing high-resolution images through electron–surface interactions. This technique enables detailed examination of surface topography and microstructural features at magnifications beyond the capabilities of optical microscopy.

Prior to analysis, the specimens were mounted on aluminium stubs and introduced into the SEM vacuum chamber to eliminate electron scattering by air molecules and ensure high-quality image acquisition. As aluminium's native oxide exhibits relatively poor electrical conductivity, the specimens were sputter-coated with a thin platinum layer using a Quorum sputter coater to minimize surface charging and improve image resolution and contrast. SEM observations were performed to evaluate the effects of the permeation tests on the specimen surface, including the presence of localized corrosion, pitting, coating degradation, hydrogen-induced surface damage, and the distribution of second-phase particles or precipitates that may act as preferential hydrogen trapping sites. The technique also enabled the assessment of the integrity of the catalytic coating following electrochemical testing and provided complementary information for interpreting the hydrogen permeation results. Images were acquired over a range of magnifications, corresponding to field widths of approximately 100–200 μm, allowing both general surface morphology and fine microstructural features to be examined in detail.

High-resolution surface characterization was performed using a Field Emission Scanning Electron Microscope (FESEM, Merlin Zeiss). The instrument is equipped with a field emission electron source, which provides a highly focused and stable electron beam, enabling imaging with excellent spatial resolution and depth of field. This makes the FESEM particularly suitable for investigating the fine surface features of aluminium alloys following hydrogen permeation testing. Prior to examination, the specimens were sputter-coated with a thin platinum layer (5 nm, Quorum sputter coater) to minimize surface charging and enhance image quality. SEM imaging was conducted using accelerating voltages between 5 and 15 kV, selected according to the desired penetration depth and image contrast. Lower accelerating voltages (5–10 kV) were employed to maximize surface sensitivity and reduce beam penetration, whereas higher voltages (up to 15 kV) were used when greater signal intensity and compositional contrast were required. The electron beam current varied between 130 pA and 1.1 nA, depending on the magnification and imaging requirements. Lower beam currents minimized beam-induced damage and charging effects, while higher currents improved the signal-to-noise ratio for detailed observation of surface morphology. These operating conditions enabled high-resolution imaging of the specimens and provided valuable information for correlating surface degradation and microstructural features with the hydrogen permeation behaviour.

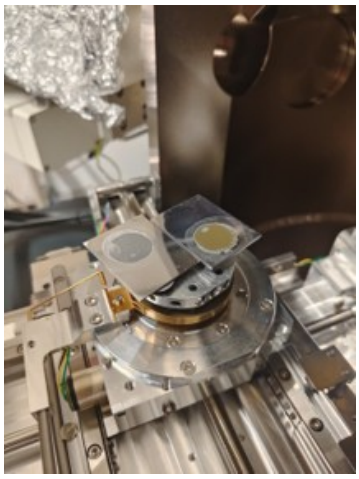

Figure 3.9: Alloy samples mounted on a sample holder to be observed under the FESEM.

Chapter 4

Results

4.1 Al-4015:

Spark analysis

The spark analysis confirmed an aluminium matrix of ≈95.681 wt%, with silicon (1.873 wt%) and iron (0.712 wt%) as the primary alloying additions, alongside magnesium (0.42 wt%) and manganese (0.847 wt%). The high Silicon content combined with the presence of iron, suggests potential for Fe-rich intermetallic phases. Iron has low solid solubility in the aluminium matrix and therefore tends to form Fe-Si intermetallic phases during solidification.

Optical Microscopy (Pristine Specimen)

The pristine samples were observed prior to permeation to evaluate the microstructural characteristics of each alloy. Cross section images are displayed in Figure **??**

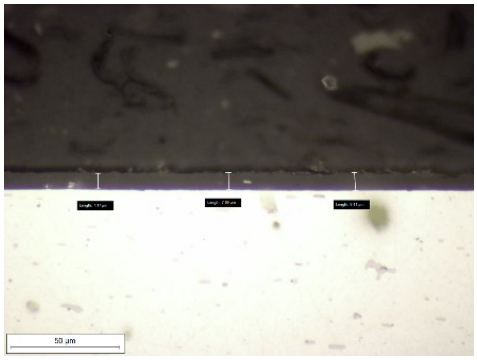

Figure 4.1: Cross section image of pristine specimen of Al-4015

The above pristine specimen were anodized specimen of the Al-4015 The presence of a small resin-metal gap of approximately 7-10 µm was observed. This separation is attributed to mounting-induced shrinkage.

The core of the sample was observed next.

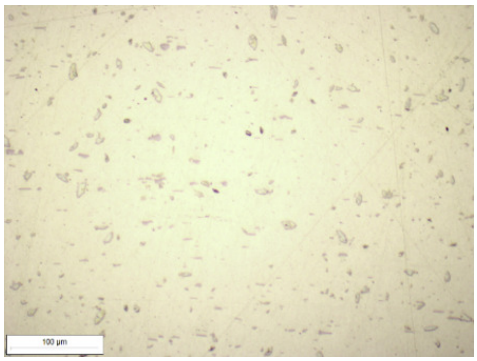

Figure 4.2: Pristine core pictures of Al-4015

Figure 4.2 is the core of the sample. The impurities within the matrix of the surface were identified as precipitates.
The specimen was coated with 30 nm of Platinum for the permeation test.

Permeation tests:

The experiment ran for a total of 53 hours. Once the current density had reached close to 986 µA/cm^2, we add the electrolyte in the cathode compartment and wait for permeation to occur. The transient current at approximately 969 µA/cm^2 was observed at about 51.08 hours from the start of the experiment.

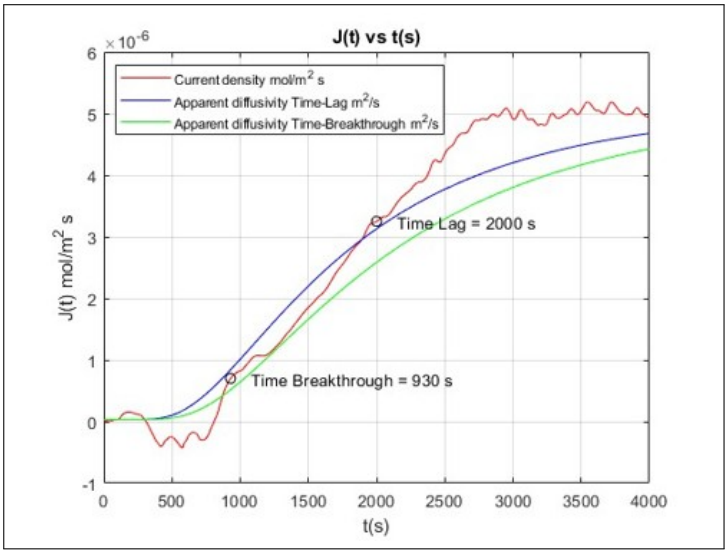

Figure 4.3: Permeation curve of Al-4015 showing Time Lag and Time Breakthrough

The graph compares the experimental hydrogen permeation transient (red curve) with the theoretical permeation curves obtained using the time-lag method (blue curve) and the breakthrough-time method (green curve) to estimate the apparent hydrogen diffusion coefficient. Initially, the current density remains close to zero and exhibits

small fluctuations associated with background noise and the stabilization of the electrochemical system. After approximately 900 seconds, the hydrogen flux begins to increase rapidly as hydrogen atoms diffuse through the specimen and reach the oxidation side of the Devanathan–Stachurski cell. The permeation current then gradually approaches a steady-state value of approximately 5×10^{-6}mol/m^{2}s, with minor oscillations resulting from experimental noise.

The green curve corresponds to the breakthrough-time model, which uses the time at which hydrogen is first detected on the exit side (t_{bt} = 930 seconds) corresponding to the initial detection of hydrogen at the exit (Anodic) surface. Although the breakthrough method characterizes the onset of hydrogen permeation, the diffusivity calculated using the breakthrough-time relationship is lower than that obtained from the time-lag method. Consequently, the predicted permeation transient rises more slowly and is shifted to longer times compared with the experimental response. Because the breakthrough method relies on the early portion of the permeation transient, it remains sensitive to experimental noise and deviations from ideal Fickian behaviour. The blue curve represents the time-lag model, which is based on the characteristic lag time of the permeation transient (t_{lag} = 2000 seconds). In this case, the time-lag calculation yields a higher apparent diffusivity than the breakthrough method, resulting in an earlier rise in the predicted permeation flux. The blue curve therefore follows the experimental transient more closely over a larger portion of the charging period. Since the time-lag method incorporates information from a greater fraction of the permeation curve, it is generally considered more representative of the overall diffusion process and less affected by local fluctuations in the initial hydrogen arrival.

The time-lag method therefore is more representative of the overall permeation process as the time-lag method focuses on a sort of delay to the steady-state conditions. This yields an apparent diffusivity that reflects real material behaviours.

From the calculations done on MATLAB, D_{app}^{tl} we obtain a value of $2.72 \times 10^{-10} m^2/s$ knowing that the lattice diffusivity of hydrogen in Aluminium is $D_l = 1.88 \times 10^{-10} m^2/s$. The Binding Energy E_b is calculated to be $3.37 \times 10^4 J/mol$ to calculate the number of traps N_T.

With the above values we could interpret that hydrogen is moving quite freely as in pure lattice diffusion with only a small fraction of it being trapped. We have evidence of this as the calculated number of traps $N_T = 2.36 \times 10^{24}/m^3$ considering the number of interstitial sites in Al-4015 is $N_L = 6.025 \times 10^{28}/m^3$. The molar trap concentration was calculated and found to be 0.0538 mol/m^3.

Microstructural analysis

Optical Microscope (Cross section)

The cross section of the samples were observed after the permeation tests.

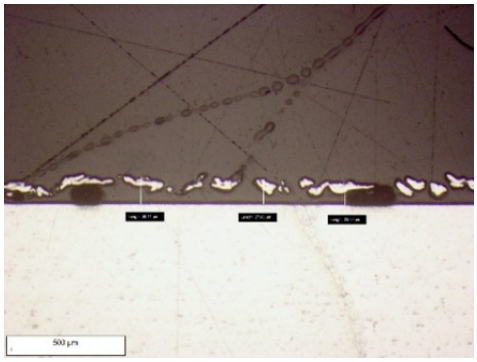

Figure 4.4: Cross section images of permeated specimen of Al-4015

Figure 4.4 represents the cross section of the Al-4015 alloy. The metallic pieces which are detached from the main metallic surface is the Platinum which has detached from the aluminium surface due to hydrogen permeating through the metal.

Optical Microscope (Surface)

The Figure 4.5a show the extensive damage to the surface of the anodic side of the Aluminium alloy. We can observe that the surface for each of the reference alloys is very irregular with cracks. It can be deduced from these pictures that the damage is caused by corrosion and material loss due to permeation.

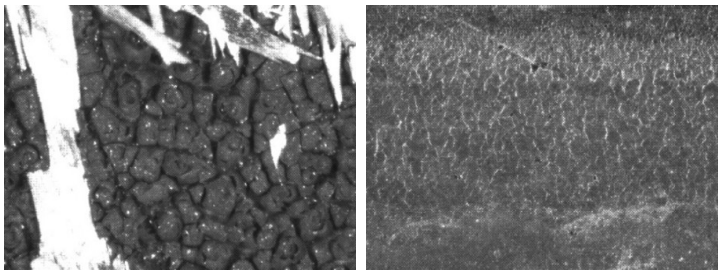

Figure 4.5: Surface of specimen after permeation. a)Anodic side of Al-4015 b)Cathodic side of Al-4015

The Figure 4.5b show the damage to the surface of the cathodic side of the Aluminium alloy. We can observe that the surface damage is not as extensive as the anodic side for each of the reference alloys. Since the cathodic side was maintained under reducing conditions associated with hydrogen charging it results in comparatively less visible deterioration.

SEM-EDS analysis

The surface and cross-section of the cathodic side of the specimen were examined at high magnification using SEM to evaluate the extent of the damage induced by the hydrogen permeation experiments. The surface exhibited numerous cracks, which are likely associated with the rupture of the native aluminium oxide film during electrochemical hydrogen charging. In addition, an apparent absence of second-phase precipitates along several grain boundaries was observed. This may indicate the detachment or dissolution of these particles during the charging process, suggesting that grain boundaries and precipitate/matrix interfaces acted as preferential sites for hydrogen accumulation. The localized enrichment of hydrogen around these microstructural features may have promoted local embrittlement, generating stress concentrations that facilitated precipitate debonding and crack initiation. As shown in Figure 4.6, the specimen also exhibits extensive degradation of the near-surface region. The dark-contrast features observed beneath the surface are likely associated with holes coming from the underlying second-phase precipitates, partially confirming the hypothesis formulated.

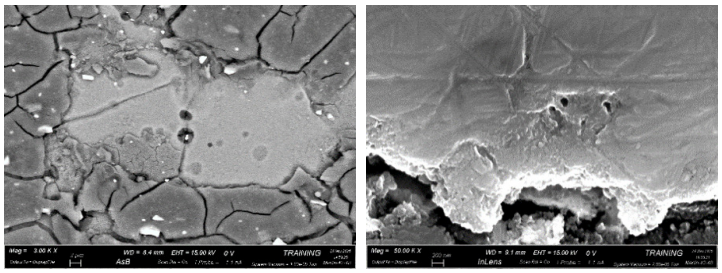

Figure 4.6: From left to right, damage caused by permeation to internal structure of specimen Al-4015 surface and cross section.

The specimen was observed under SEM and EDS analysis was performed on the cathodic side of the specimen as it can reveal the segregation of the alloying elements and possible sites associated with hydrogen trapping.
Site 1 was taken at 10 µm scale at 1000× magnification:

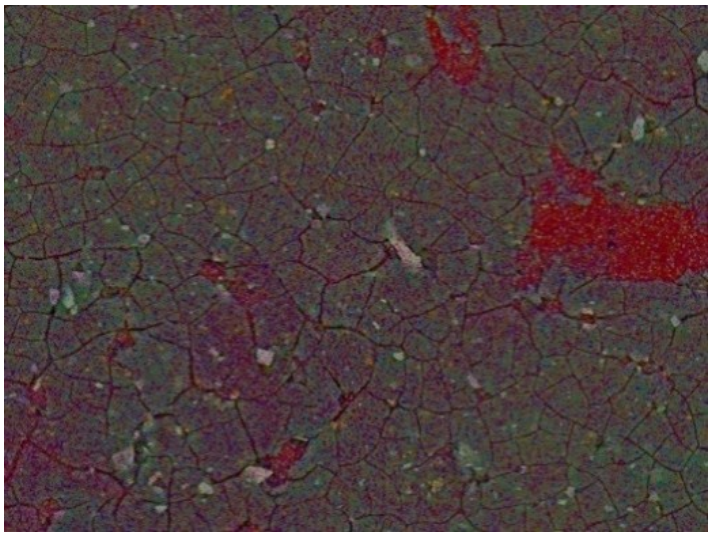

Figure 4.7: EDS Layered image of cathode side of Al-4015 after hydrogen permeation testing.

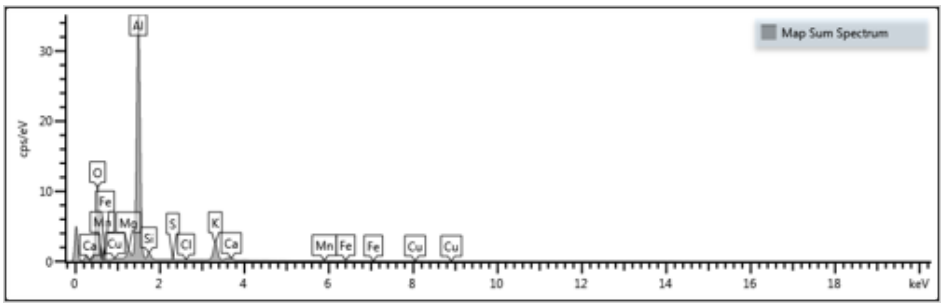

Figure 4.8: EDS map-sum spectrum of the analyzed region after hydrogen permeation testing, showing the characteristic peaks corresponding to aluminium, oxygen, and minor alloying elements.

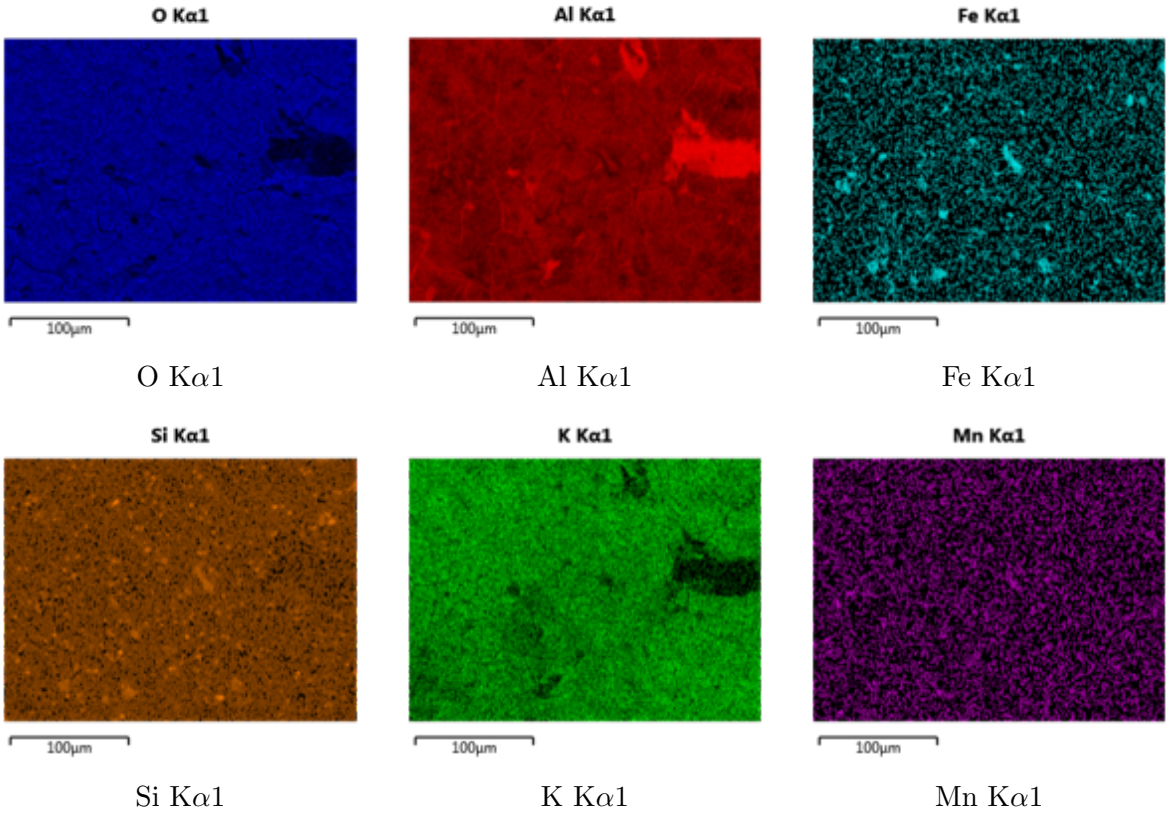

Figure 4.9: EDS elemental maps of the Al-4015 alloy after hydrogen permeation testing, showing the distribution of O, Al, Fe, Si, K and Mn across the analyzed surface region.

The EDS elemental map in Figure 4.7 shows the different characteristic elements present in the region. The presence of Potassium K (green) and Oxygen O (blue) can be attributed to the KOH electrolyte. Aluminium Al (red) is concentrated in the underlying area of the oxide layer. Iron Fe (light blue) and Silicon Si (orange) are found scattered throughout the region where the two elements appear to be co-localized. We can assume that Fe-Si intermetallic sites exist within the matrix of the specimen which could act as hydrogen traps. The Manganese Mn (magenta) is much more scattered than Fe or Si but is concentrated more the regions of higher concentrations of Fe and Si. We can also assume that Mn is a constituent within the Fe-Si intermetallic site but of lesser concentrations.

Table 4.1: Quantitative EDS results showing the elemental composition of the analyzed region of the Site 1 of Al-4015 alloy after permeation testing.

Element	Atomic %	Weight %
O	57.58	43.29
Mg	1.37	1.56
Al	35.26	44.70
Si	1.29	1.70
S	0.06	0.09
Cl	0.02	0.04
K	3.46	6.35
Ca	0.38	0.71
Mn	0.19	0.50
Fe	0.33	0.86
Cu	0.07	0.20
Total	100.00	100.00

In Table 4.1, O (43.29 wt%) and K (6.35 wt%) are attributed to the KOH electrolyte used in the experiment. The relatively high Mg (1.56 wt%) content present in the region is due to EDS analysis representing a localized surface measurement, the measured Mg concentration reflects the composition if the analyzed area and should not be interpreted as the nominal bulk alloy composition. The intermetallic elements Fe (0.86 wt%), Si (1.70 wt%) and Mn (0.50 wt%) respectively, along with the corresponding elemental maps can be interpreted as the elements associated with Fe-Si-Mn rich features which may influence hydrogen transport behaviour through the creation of local trapping sites.

Site 2 was taken at 3 µm scale at 3000x magnification to inspect a region in Site 1 more closely and with greater detail:

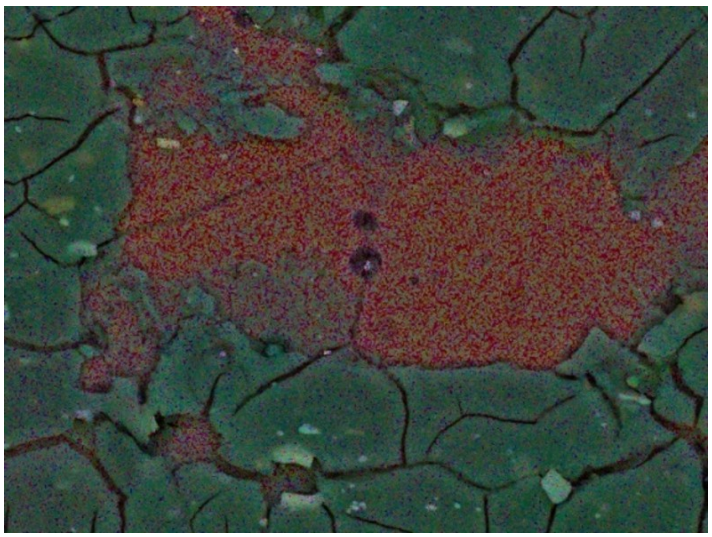

Figure 4.10: EDS Layered image of Site 2 of Al-4015 after hydrogen permeation testing

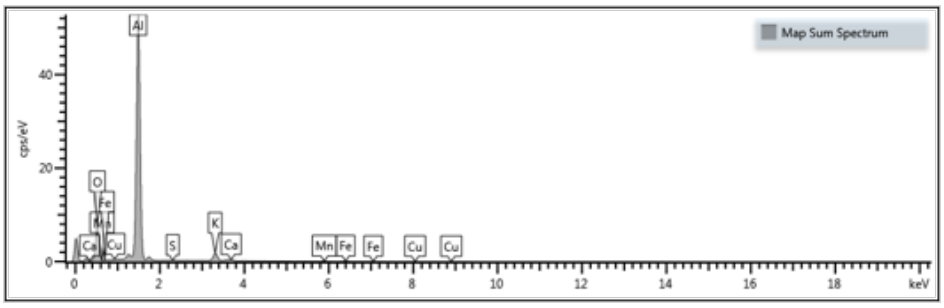

Figure 4.11: EDS map-sum spectrum of the analyzed region after hydrogen permeation testing, showing the characteristic peaks corresponding to aluminium, oxygen, and minor alloying elements.

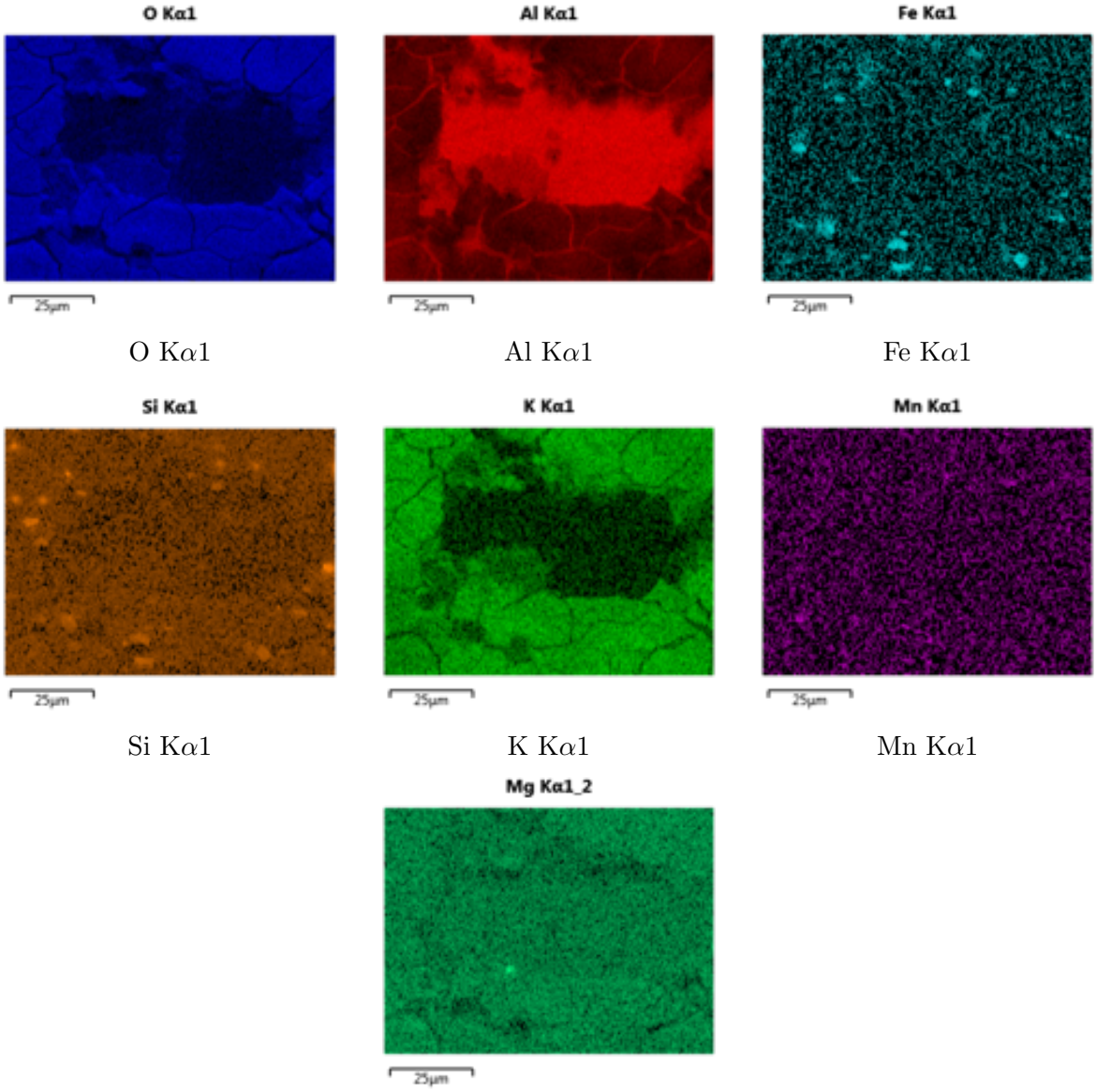

O Kα1 Al Kα1 Fe Kα1

Si Kα1 K Kα1 Mn Kα1

Mg Kα1

Figure 4.12: EDS elemental maps of the Al-4015 alloy after hydrogen permeation testing, showing the distribution of O, Al, Fe, Si, K, Mn, Fe and Mg across the analyzed surface region.

In Figure 4.10, the EDS elemental map shows similar characteristics of the elements in the region as Figure 4.12. In the above region, Potassium K (green) and Oxygen O (blue) are not present in the region of pure Aluminium Al (red) which could be interpreted as the Aluminium Oxide layer over pure Aluminium. Iron Fe (light blue) and Silicon Si (orange) are co-localized similar to Site 1. Manganese Mn (magenta) and Magnesium Mg (dark green) are present but scattered throughout the matrix of the specimen, Mn being relatively more concentrated in the regions of co-localized Fe-Si sites.

These second phase constituents are situated predominantly on the oxide layer of the alloy and not in the underlying Aluminium as seen in Figure 4.7. They are situated adjacent to cracks in the oxide layer. These precipitates appear to be in an irregular quadrilateral shape.

Table 4.2: Quantitative EDS results showing the elemental composition of the analyzed region of the Site 2 of Al-4015 alloy after permeation testing.

Element	Atomic %	Weight %
O	46.37	33.17
Mg	-	-
Al	50.33	60.71
Si	-	-
S	0.05	0.07
Cl	-	-
K	2.38	4.17
Ca	0.42	0.75
Mn	0.13	0.33
Fe	0.23	0.57
Cu	0.08	0.24
Total	100.00	100.00

In Table 4.2, we find a similar trend of the concentration of elements like that of Site 1. The first obvious indication is the higher concentration of Al, O and K by weight percentage (60.71 wt%, 33.17 wt% and 4.17 wt% respectively). Although Si was not detected in the point analysis in Table 4.2, the elemental maps in Figure 4.12 confirmed the presence of silicon within the analyzed region. This discrepancy highlights the localized nature of point EDS measurements and suggests that Site 2 was in an area with a low silicon concentration compared to surrounding Si-containing features. Fe and Mn (0.57 wt% and 0.33 wt% respectively) is consistent with the weight percentage as Site 1 suggests that both locations contain similar Fe-Mn microstructural constituents.

Calculation of volume fraction of precipitates

The thickness of the alloy was measured using a Vernier Caliper, the lattice diffusivity and lattice parameter are predetermined values of the metallic properties of Aluminium. The Volume fraction and Mean Area of precipitate was found in Image J analysis of a region of the alloy.

The Mean precipitate radius r in Table 4.4 was measured at 1.767 μm. From this, the interfacial area per unit volume S_v was calculated to be $0.068 \times 10^6 \mathrm{m}^2/\mathrm{m}^3$. Using the FCC-Al (111) planar atomic density, these stereological measurements yield a geometric trap density N_T^{geo} of $6.79 \times 10^2 2\mathrm{traps/m}^3$. This value represents the trap density predicted from precipitate morphology and interfacial area alone, and can be compared against the trap density N_T obtained independently from permeation curve fitting to assess whether interfacial trapping accounts for the observed hydrogen trapping behavior.

Table 4.3: Parameters used for geometric trap density calculations.

Parameter	Symbol	Value
Specimen thickness	L	1.25×10^{-3} m
Lattice diffusivity	D_L	1.88×10^{-10} m^2/s
Lattice parameter	a	4.049×10^{-10} m
Volume fraction	V_f	4 %
Mean precipitate area	$\overline{A}$	9.8 μm^2

Table 4.4: Calculated stereological parameters and geometric trap density.

Parameter	Symbol	Value
Mean precipitate radius	r	1.767 μm
Interfacial area per unit volume	S_V	0.068×10^6 m^2/m^3
Geometric trap density	N_T^{geo}	6.79×10^{22} traps/m^3

The presence of potential trapping sites is further strengthened by the EDS analysis in Figures 4.7 and 4.10. They show substantial density of the Fe-Si intermetallic precipitates.

4.2 Al-5083:

Spark Analysis

The spark analysis identified magnesium as the dominant alloying element at 4.53–4.68 wt%, with aluminium constituting the balance at ≈94.2 wt%. Trace quantities of silicon (0.06 wt%) and copper (0.006 wt%) confirmed the non-heat-treatable nature of this alloy. Manganese (0.83 wt%) and chromium (0.085 wt%) were identified as

dispersoid-forming additions. The composition closely corresponds to alloy 5083, and the magnesium content exceeding 3.5 wt% is of particular significance, as it renders this alloy susceptible to β-phase (Al_3Mg_2) sensitization at grain boundaries — a condition directly associated with intergranular hydrogen embrittlement.

Optical Microscope (Pristine Specimen)

The pristine samples were observed prior to permeation to evaluate the microstructural characteristics of each alloy. Cross section images are displayed in Figure 4.13

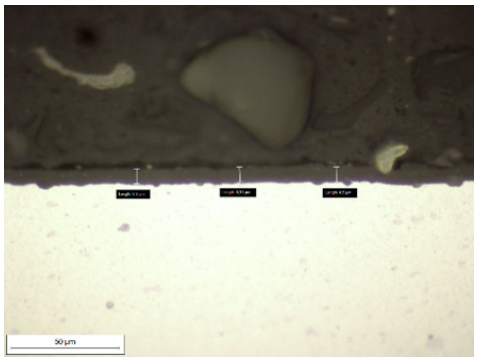

Figure 4.13: Cross section image of pristine specimen of Al-5083

The above pristine specimen were anodized specimen of the Al-5083 The presence of a small resin-metal gap of approximately 7-10 µm was observed. This separation is attributed to mounting-induced shrinkage.

The core of the sample was observed next.

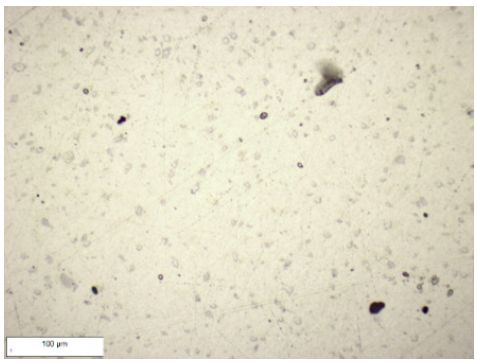

Figure 4.14: Pristine core pictures of Al-5083

Figure 4.14 is the core of the sample. The impurities within the matrix of the surface were identified as precipitates.
The specimen was coated with 30 nm of Platinum for the permeation test.

Permeation tests

The experiment ran for a total of 70 hours. Once the current had reached close to 380 µA/cm^2, we add the electrolyte in the cathode compartment and wait for permeation to occur. The transient current at approximately 383 µA/cm^2 was observed at about 67.42 hours from the start of the experiment.

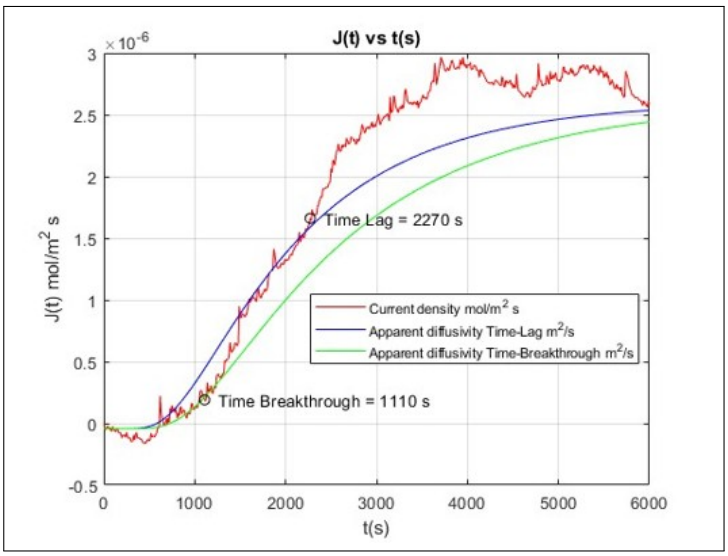

Figure 4.15: Permeation curve of Al-5083 showing Time Lag and Time Breakthrough

As with Figure 4.15, the graph compares the experimental hydrogen permeation transient (red curve) with the theoretical permeation curves obtained using the time-lag method (blue curve) and the breakthrough-time method (green curve) to estimate the diffusion coefficient. In Figure 4.15 the transient is noticeably more noisy and slower. After close to 3500 seconds the current density stabilizes between 3 - 2.5 $\times 10^{-6}$mol/m^{2}s.

From the calculations done on MATLAB, D_{app}^{tl} we obtain a value of 1.09×10^{-10}m^2/s knowing that the lattice diffusivity of hydrogen in Aluminium is $D_l = 1.88 \times 10^{-10}$m^2/s. The Binding Energy E_b is calculated to be 9.64×10^4J/mol to calculate the number of traps N_T.

The Time Lag is longer at 2270 seconds. This indicates an overall moderate trapping behaviour.

We have the calculated number of traps $N_T = 5.401 \times 10^{11}$/m3 considering the number of interstitial sites in Al-5083 is $N_L = 6.025 \times 10^{28}$/m3. The molar trap concentration was calculated and found to be 8.97×10^{-13}mol/m3.

Microstructural analysis

Optical Microscope (Cross section)

The cross section of the samples were observed after the permeation tests.

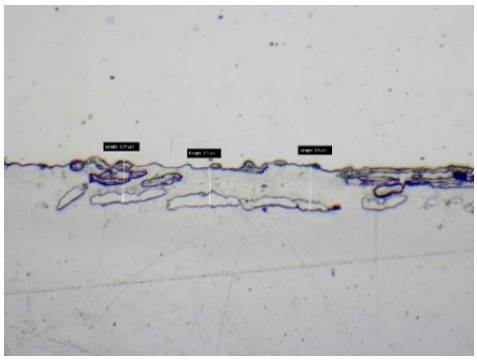

Figure 4.16: Cross section images of permeated specimen of Al-5083

Similar to Figure 4.4, Figure 4.16 shows the Platinum detached from the surface of the metal surface after permeation. The Platinum layer appears more discontinuous than the Al-4015 specimen.

Optical Microscope (Surface)

The Figure 4.17a show the extent of the damage to the surface of the anodic side of the Aluminium alloy. The surface of the reference alloy is very irregular with cracks but not as severe as the surface of Al-4015 in Figure 4.5. It is certain that the damage has been caused by corrosion and material loss due to permeation.

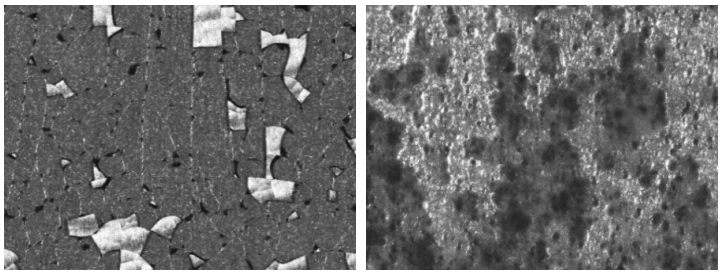

Figure 4.17: Surface of specimen after permeation. a)Anodic side of Al-5083 b)Cathodic side of Al-5083

Figure 4.17b shows the surface of the cathodic side of the Aluminium alloy. The surface appears to have deep pits within the surface of the alloy. This could be due to hydrogen induced pitting of the surface or dissolution of the β-phase (Mg_2Al_3)

SEM-EDS Analysis

The surface and cross-section of the cathodic side of the specimen were examined at high magnification using SEM to evaluate the extent of the damage induced by the hydrogen permeation experiment. The surface does not appear to have any major damage at first but the native oxide layer has numerous cracks throughout the matrix of the alloy. The cracks along the surface appear to follow an intergranular path, which

is consistent with intergranular hydrogen assisted cracking rather than transgranular fracture.

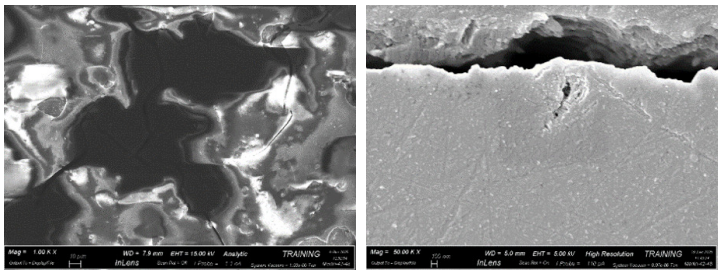

Figure 4.18: From left to right, damage caused by permeation to internal structure of specimen Al-5083, surface and cross section

The specimen was observed under SEM and EDS analysis was performed on the cathodic side of the specimen as it can reveal the segregation of the alloying elements and possible sites associated with hydrogen trapping.
Site 1 was taken at 10 µm at 1000× magnification:

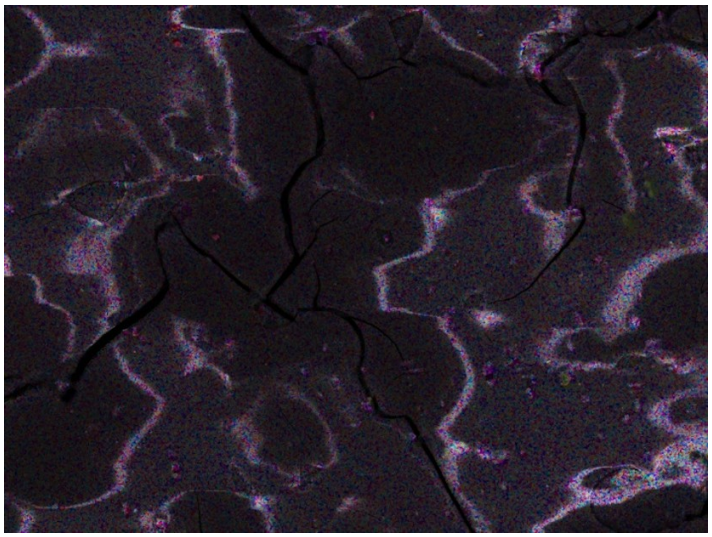

Figure 4.19: EDS Layered image of Site 1 of Al-5083 after hydrogen permeation testing.

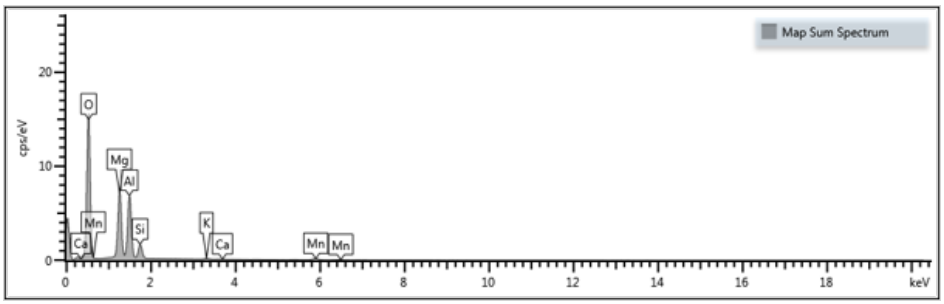

Figure 4.20: EDS map-sum spectrum of the analyzed region after hydrogen permeation testing, showing the characteristic peaks corresponding to aluminium, magnesium, and minor alloying elements.

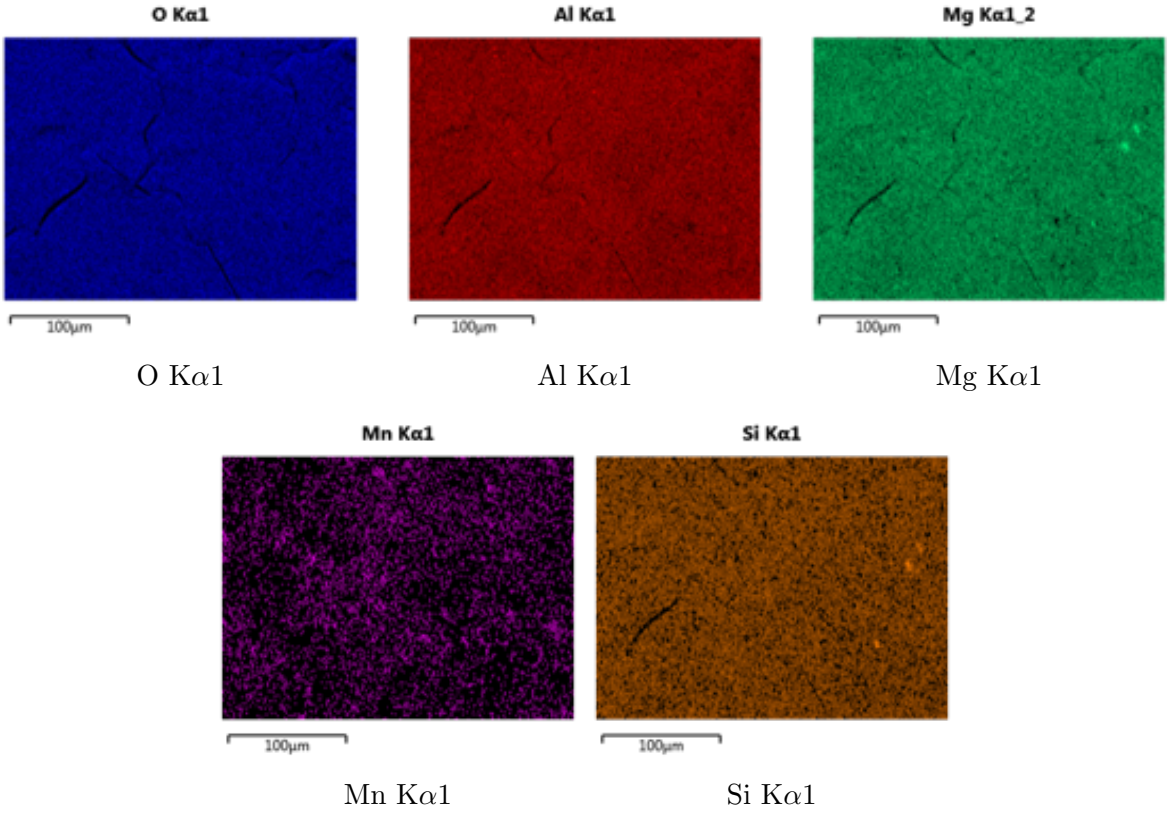

Figure 4.21: EDS elemental maps of the Al-5083 alloy after hydrogen permeation testing, showing the distribution of O, Al, Fe, Si, Mn and Mg across the analyzed surface region.

The EDS elemental map in Figure 4.21 shows the different characteristic elements present in the particular region. The presence of Oxygen O (blue) can be attributed to the KOH electrolyte. Aluminium Al (red) in the underlying area of the oxide layer of Aluminium Oxide. Silicon Si (orange) and Magnesium Mg (dark green) are found scattered throughout the region aside from two or three well concentrated regions in the right of the image, where the two elements appear to be co-localized. We can assume that Mg-Si intermetallic sites exist within the matrix of the specimen which could act as hydrogen traps. The Manganese Mn (magenta) is much more scattered and is evenly distributed within the matrix rather than concentrated points.

Table 4.5: Quantitative EDS results showing the elemental composition of the analyzed region of the Site 1 of Al-5083 alloy after permeation testing.

Element	Atomic %	Weight %
O	72.08	60.76
Mg	12.57	16.10
Al	11.73	16.68
Si	2.69	3.99
K	0.16	0.32
Ca	0.06	0.12
Mn	0.70	2.03
Total	100.00	100.00

In Table 4.5, O (60.76 wt%) and K (0.32 wt%) are attributed to the KOH electrolyte used in the experiment. The high O weight percentage could indicate that the analyzed area was dominated by surface oxide rather than the metallic alloy matrix. The high Mg (16.10 wt%) content present in the region corresponds to a Mg-enriched surface feature. The intermetallic elements Mg and Si (3.99 wt%), along with the corresponding elemental maps can be interpreted as the elements associated with Mg-Si rich features which may influence hydrogen transport behaviour through the creation of local trapping sites.

Calculation of the volume fraction of precipitates

The thickness of the alloy was measured using Vernier Caliper, the lattice diffusivity and lattice parameter are predetermined values of the metallic properties of Aluminium. The Volume fraction and Mean Area of precipitate was found in Image J analysis of a region of the alloy.

The Mean precipitate radius r in Table 4.7 was measured at 0.67 μ. From this, the interfacial area per unit volume S_v was calculated to be 0.049 $\times 10^6 \mathrm{m}^2/\mathrm{m}^3$. Using the FCC-Al (111) planar atomic density, these stereological measurements yield a geometric trap density N_T^{geo} of 4.88 $\times 10^{22} traps/m^3$. Al-5083 shows a smaller mean precipitate radius but a lower interfacial area per unit volume and a somewhat lower geometric trap density. Since interfacial trap density depends on both precipitate size and number density/distribution, this suggests the two microstructures differ not just in precipitate size but also in how finely or densely those precipitates are distributed through the matrix.

Table 4.6: Parameters used for geometric trap density calculations.

Parameter	Symbol	Value
Specimen thickness	L	1.22×10^{-3} m
Lattice diffusivity	D_L	1.88×10^{-10} m^2/s
Lattice parameter	a	4.049×10^{-10} m
Volume fraction	V_f	1.09 %
Mean precipitate area	$\overline{A}_{\text{precipitate}}$	1.41 μm^2

Table 4.7: Calculated stereological parameters and geometric trap density of Al-5083.

Parameter	Symbol	Value
Mean precipitate radius	r	0.67 μm
Interfacial area per unit volume	S_V	0.049×10^6 m^2/m^3
Geometric trap density	N_T^{geo}	4.88×10^{22} traps/m^3

The Table 4.7 suggests that factors other than particle–matrix interface density contribute significantly to trapping behaviour. In particular, Mg-rich phases and solid-solution Mg atoms present in Al-5083 may provide favourable trapping sites.

4.3 Al-6016:

Spark Analysis

The spark analysis confirmed a composition of ≈97.9 wt% aluminium, with silicon (1.06 wt%) and magnesium (0.40 wt%) as the principal alloying elements. Minor additions of iron (0.29 wt%), manganese (0.14 wt%), and chromium (0.025 wt%) were also detected. The Si:Mg ratio is consistent with alloys 6016 which is commonly used in automotive structural applications.

Optical Microscope (Pristine Specimen)

The pristine samples were observed prior to permeation to evaluate the microstructural characteristics of each alloy. Cross section images are displayed in Figure 4.22

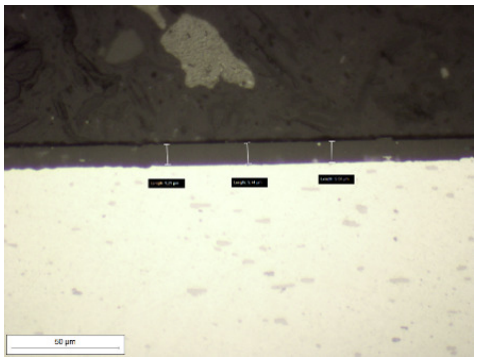

Figure 4.22: Cross section images of pristine specimen of Al-6016.

The above pristine specimen were anodized specimen of the Al-6016 alloy. The presence of a small resin-metal gap of approximately 7-10 µm was observed. This separation is attributed to mounting-induced shrinkage.

The core of the sample was observed next.

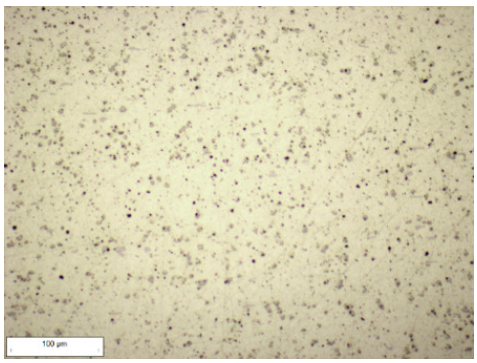

Figure 4.23: Pristine surface pictures of Al-6016.

Figure 4.23 is the core of the sample. The impurities within the matrix of the surface were identified as precipitates and it was observed to have more precipitates within the same area as the other alloys.

Permeation tests

The experiment ran for a total of 51.9 hours. Once the current had reached close to 520 µA/cm^2, we add the electrolyte in the cathode compartment and wait for permeation to occur. The transient current at approximately 524 µA/cm^2 was observed at about 45.3 hours from the start of the experiment.

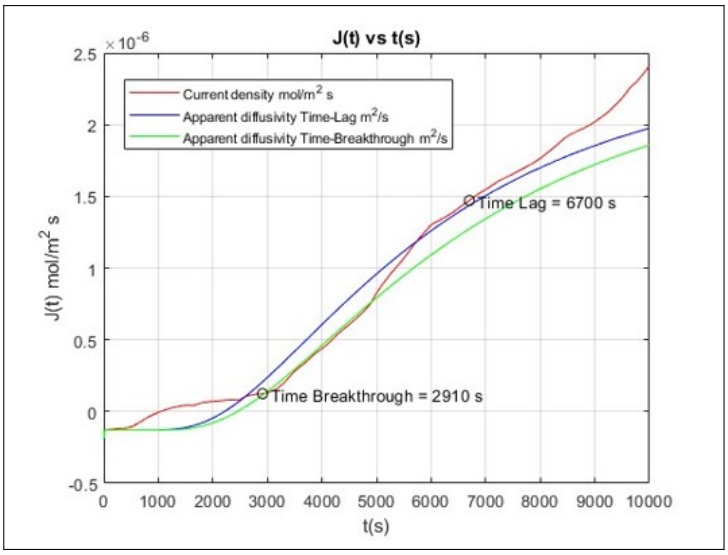

Figure 4.24: Permeation curve of Al-6016 showing Time Lag and Time Breakthrough

In Figure 4.24, the graph compares the experimental hydrogen permeation transient (red curve) with the theoretical permeation curves obtained using the time-lag method (blue curve) and the breakthrough-time method (green curve) to estimate the diffusion coefficient. In Figure 4.24 the transient appears to gradually rise until it reaches a current density of around 2.4 $\times 10^{-6}$mol/m^{2}s. The transient is noticeably slower. It had a lot of fluctuations, therefore, to mitigate the fluctuations a filter was applied in MATLAB to smoothen the curve by a large degree.

From the calculations done on MATLAB, D_{app}^{tl} we obtain a value of 2.69×10^{-11}m^2/s knowing that the lattice diffusivity of hydrogen in Aluminium is $D_l = 1.88\times10^{-10}$m^2/s. The Binding Energy E_b is calculated to be 2.005×10^5J/mol to calculate the number of traps N_T.

The Time Lag is longer at 6700 seconds. This indicates an overall high trapping behaviour. We have the calculated number of traps $N_T = 2.57 \times 10^{-6}$/m^3 considering the number of interstitial sites in Al-6016 is $N_L = 6.025 \times 10^{28}$/m^3. The molar trap concentration was calculated and found to be 4.27×10^{-30}mol/m^3.

Microstructual Analysis

Optical Microscope (Cross section)

The cross section of the samples were observed after the permeation tests.

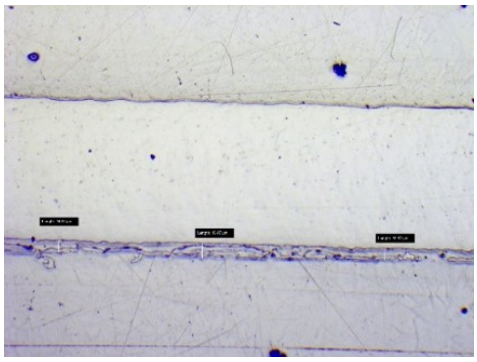

Figure 4.25: Cross section images of permeated specimen of Al-6016

Figure 4.25 again shows the Platinum layer is detached from the metal. The layer has not detached completely from the surface of the alloy but appears more as a continuous layer compared to Al-4015 and much more in comparison to Al-5083

Optical Microscope (Surface)

The Figure 4.26a shows the extent of the damage of the anodic side of the Aluminium alloy. The surface has deep pits which are a similar to the Al-5083 alloy. This could indicate hydrogen induced pitting of the surface or dissolution of the secondary phase elements.

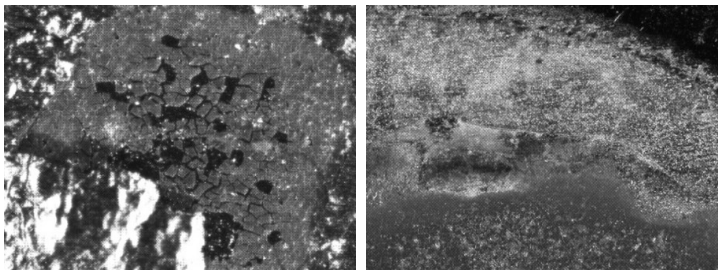

Figure 4.26: Surface of specimen after permeation a) Anodic side of Al-6016 b) Cathodic side of Al-6016

The Figure 4.26b shows the cathodic side of the Aluminium alloy. The surface appears relatively intact except for corrosion of the metal oxide.

SEM-EDS Analysis

The surface and the cross section of the cathodic side of the specimen were examined at high magnification using SEM to evaluate the extent of the damage induced by the hydrogen permeation experiment. Figure 4.27 shows a large pit where the oxide layer has been lost and cracks can be found within the underlying matrix. A large number of precipitates can be observed throughout the region. In Figure 4.27b, we can observe dark patches on the metallic surface which could indicate the underlying precipitates in the matrix of the specimen.

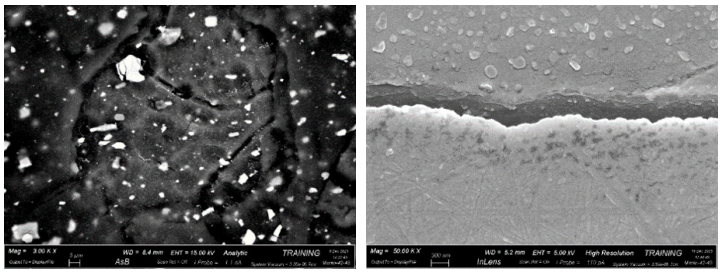

Figure 4.27: From left to right, damage caused by permeation to internal structure of specimen Al-6016, surface and cross section.

The specimen was observed under SEM and EDS analysis was performed on the cathodic side of the specimen as it can reveal the segregation of the alloying elements and possible sites associated with hydrogen trapping.
Site 1 was taken at 10 µm scale at 1000× magnification:

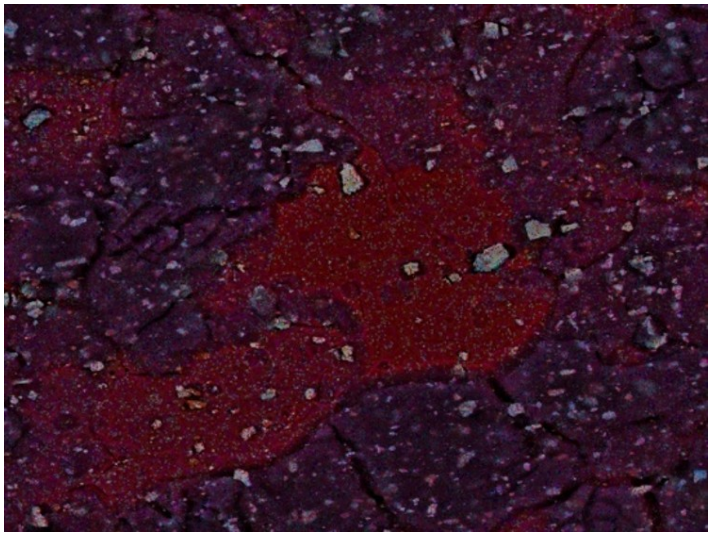

Figure 4.28: EDS Layered image of Site 1 of Al-6016 after hydrogen permeation testing.

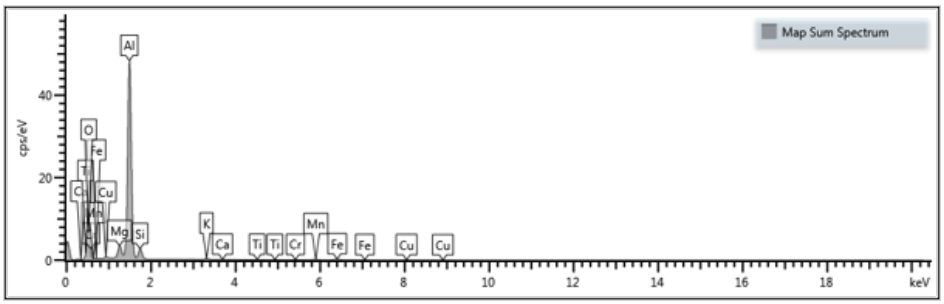

Figure 4.29: EDS map-sum spectrum of the analyzed region after hydrogen permeation testing, showing the characteristic peaks corresponding to aluminium, iron, and minor alloying elements.

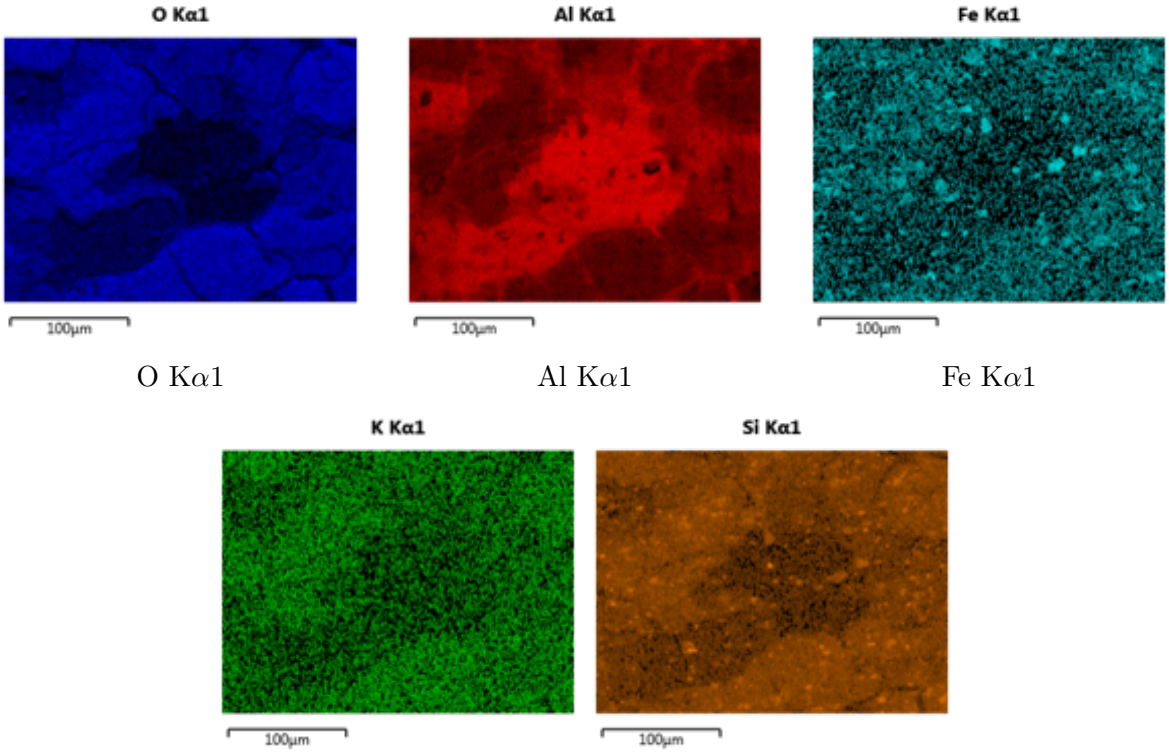

Figure 4.30: EDS elemental maps of the Al-6016 alloy after hydrogen permeation testing, showing the distribution of O, Al, K, Fe and Si across the analyzed surface region.

The EDS elemental map in Figure 4.30 shows the different characteristic elements present in the particular region. The presence of Oxygen O (blue) and Potassium K (green) can be attributed to the KOH electrolyte. Aluminium Al (red) in the underlying area of the oxide layer of Aluminium Oxide. Silicon Si (orange) and Iron Fe (light blue) are found scattered throughout the region aside from two or three well concentrated regions, where the two elements appear to be co-localized, although the concentration of Fe is higher than Si. We can assume that Fe-Si intermetallic sites exist within the matrix of the specimen which could act as hydrogen traps like the Al-4015.

Table 4.8: Quantitative EDS results showing the elemental composition of the analyzed region of the Site 1 of Al-6016 alloy after permeation testing.

Element	Atomic %	Weight %
O	39.41	27.07
Mg	3.38	3.53
Al	50.58	58.58
Si	4.15	5.00
K	0.29	0.49
Ca	0.06	0.10
Ti	0.07	0.14
Cr	0.10	0.23
Mn	0.54	1.26
Fe	0.94	2.25
Cu	0.50	1.36
Total	100.00	100.00

In Table 4.8, Iron Fe (2.25 wt%) and Silicon Si (5.00 wt%) are present in relatively high percentage. Along with the elemental maps, it can be interpreted as Fe-Si intermetallic sites which may influence hydrogen transport by providing potential trapping sites.

Site 2 was taken at 3 µm scale at 3000x magnification:

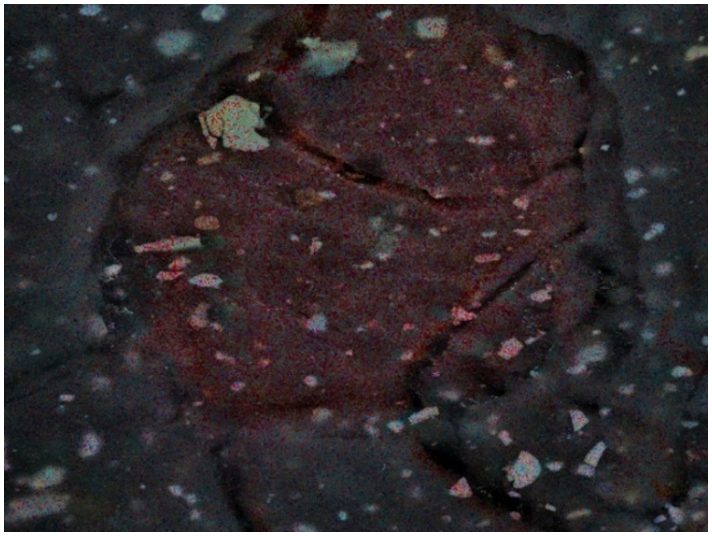

Figure 4.31: EDS Layered image of Site 2 of Al-6016 after hydrogen permeation testing.

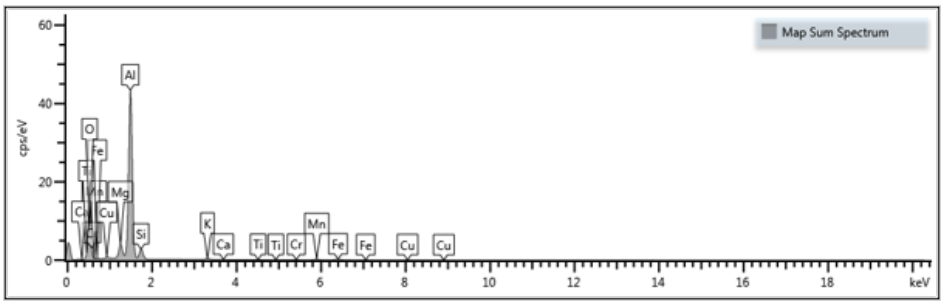

Figure 4.32: EDS map-sum spectrum of the analyzed region after hydrogen permeation testing, showing the characteristic peaks corresponding to aluminium, iron, and minor alloying elements.

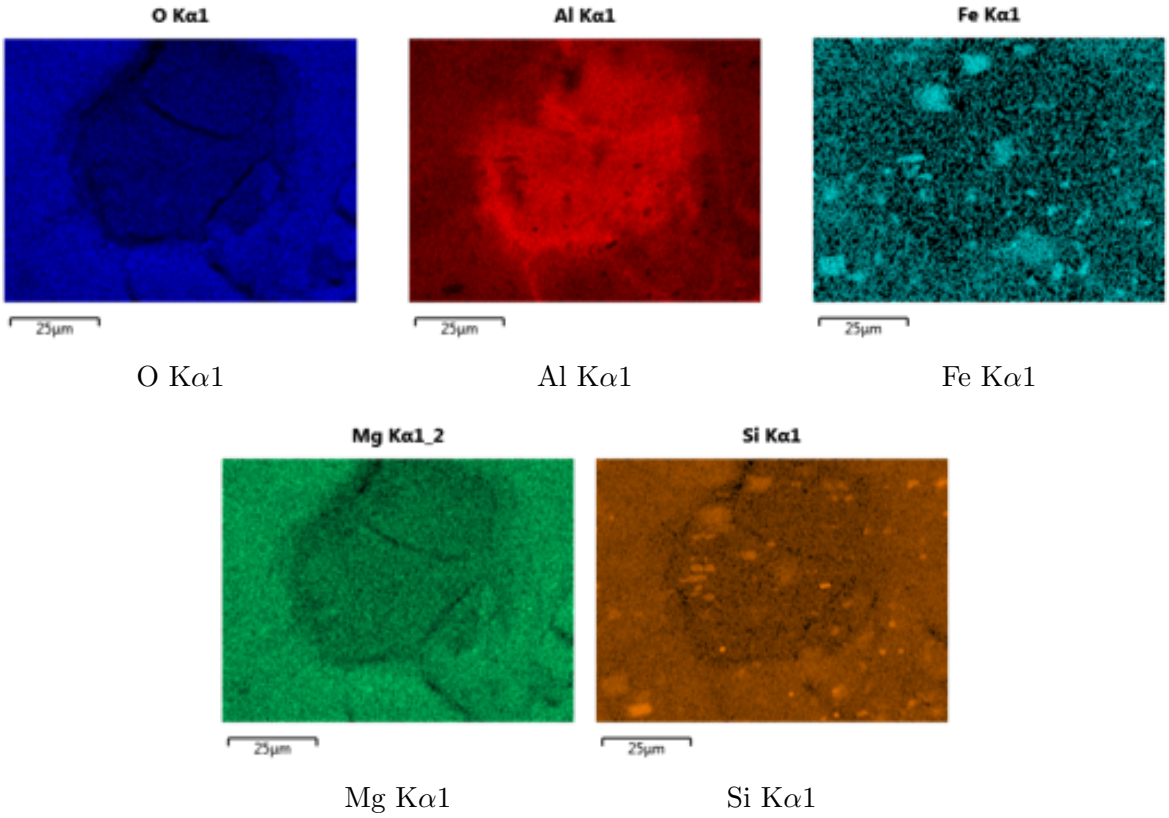

O Kα1 Al Kα1 Fe Kα1

Mg Kα1 Si Kα1

Figure 4.33: EDS elemental maps of the Al-6016 alloy after hydrogen permeation testing, showing the distribution of O, Al, K, Fe and Si across the analyzed surface region.

In Figure 4.33, the elemental maps suggest that Magnesium Mg (dark green) is present in the bulk of the alloy rather than a localized region. The elements which are co-localized are mainly Iron Fe (light blue) and Silicon Si (orange) which are present around and within the Aluminium Al (red) matrix of the alloy.

The second-phase precipitates appear to be numerous and are present within the Aluminium matrix rather than just on the Aluminium Oxide layer like the Al-4015 in Figure 4.10. The precipitates are also larger in size and may contribute to the longer

permeation transient. The precipitates appear irregular in shape but there are a few which are rectangular in shape.

Table 4.9: Quantitative EDS results showing the elemental composition of the analyzed region of the Site 2 of Al-6016 alloy after permeation testing.

Element	Atomic %	Weight %
O	43.37	30.32
Mg	4.03	4.29
Al	45.83	54.04
Si	4.12	5.06
K	0.33	0.56
Ca	0.06	0.11
Ti	0.06	0.13
Cr	0.13	0.29
Mn	0.61	1.46
Fe	0.90	2.20
Cu	0.56	1.55
Total	100.00	100.00

In Table 4.9, EDS analysis suggests the concentrations of Fe (2.20 wt%) and Si (5.06 wt%) are consistent with the concentrations of these elements in Site 1. We can infer from these comparisons that the concentration of Fe-Si intermetallic traps are homogeneous within the matrix of the alloy.

Calculation of the volume fraction of precipitates

The thickness of the alloy was measured using Vernier Caliper, the lattice diffusivity and lattice parameter are predetermined values of the metallic properties of Aluminium. The Volume fraction and Mean Area of precipitate was found in Image J analysis of a region of the alloy.

The Mean precipitate radius r in Table 4.11 was measured at 1.207 μm. From this, the interfacial area per unit volume S_v was calculated to be 0.113 $\times 10^6 \mathrm{m}^2/\mathrm{m}^3$. Using the FCC-Al (111) planar atomic density, these stereological measurements yield a geometric trap density N_T^{geo} of 1.13 $\times 10^{22} traps/m^3$. The relatively high geometric trap density supports the permeation measurements, where Al-6016 exhibited the lowest apparent diffusivity among the wrought alloys. The abundance of precipitate–matrix interfaces increases the probability of hydrogen being temporarily trapped during diffusion, thereby prolonging transport through the material and reducing the effective hydrogen mobility. This indicates that the microstructure of Al-6016 provides a greater density of reversible trapping sites than Al-4015 and Al-5083.

Table 4.10: Analysis of Geometric Trap density for Al-6016.

Parameter	Symbol	Value
Specimen thickness	L	1.04×10^{-3} m
Lattice diffusivity	D_L	1.88×10^{-10} m^2/s
Lattice parameter	a	4.049×10^{-10} m
Volume fraction	V_f	4.54 %
Mean precipitate area	$\overline{A}_{\text{precipitate}}$	4.576 μm^2

Table 4.11: Calculated stereological parameters and geometric trap density of the analyzed alloy.

Parameter	Symbol	Value
Mean precipitate radius	r	1.207 μm
Interfacial area per unit volume	S_V	0.113×10^6 m^2/m^3
Geometric trap density	N_T^{geo}	1.13×10^{23} traps/m^3

4.4 A319 (Engine Head)

For this thesis a variant of the Al-4xxx alloy, particularly 319 (Al-Si-Cu) casting alloy [21] was used as it is one the most widely used alloys in the automotive industry to cast engine heads. Chemical analysis of the cylinder head specimens was carried out using optical emission spectroscopy (spark analysis). The composition was contained approximately 5.5–6.5 wt% Si, 3–4 wt% Cu, and 0.2–0.5 wt% Mg, with aluminium forming the balance of the alloy. Minor quantities of Fe, Mn, and Ni were also detected.

Permeation tests

The experiment ran for a total of 71.4 hours. Once the current had reached close to 404 µA/cm^2, we add the electrolyte in the cathode compartment. As soon as the KOH electrolyte was added the current rose significantly as seen in Figure 4.34. We then waited for the flux to reach steady state, and it did so after 15 minutes of adding the KOH solution. The transient current at approximately 353 µA/cm^2 was observed at about 67.7 hours from the start of the experiment.

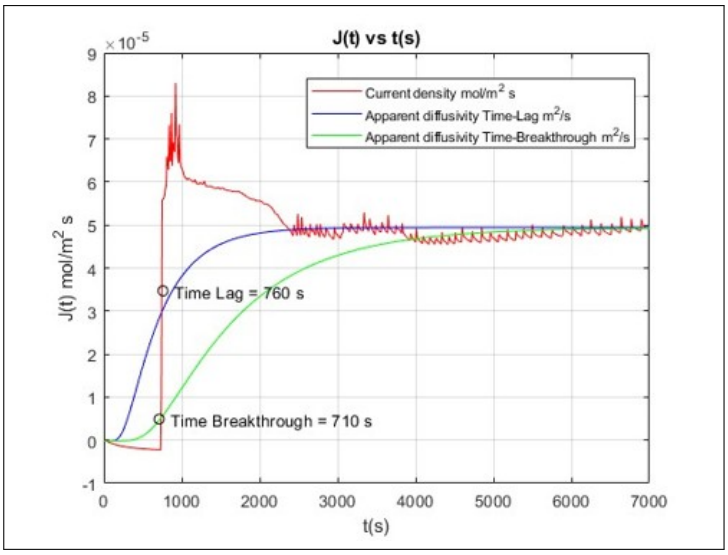

Figure 4.34: Permeation curve of A319 (Engine Head) showing Time Lag and Time Breakthrough

The graph compares the experimental hydrogen permeation transient (red curve) with the theoretical permeation curves obtained using the time-lag method (blue curve) and the breakthrough-time method (green curve) to estimate the diffusion coefficient. In Figure 4.34, the transient is extremely quick given by the Time Lag at 760 seconds which indicates that the hydrogen transport was only minimally delayed by trapping during the initial stages of permeation. The current density then drops until it reaches a stable value of 5 $\times 10^{-5}$mol/m^{2}s.

From the calculations done on MATLAB, D_{app}^{tl} we obtain a value of $9.55 \times 10^{-11} m^2/s$ knowing that the lattice diffusivity of hydrogen in Aluminium is $D_L = 1.88 \times 10^{-10} m^2/s$. The Binding Energy E_b is calculated to be 3.37×10^4J/mol to calculate the number of traps N_T.

We have the calculated number of traps $N_T = 7.06 \times 10^{22}$/m^3 considering the number of interstitial sites in A319 (Engine Head) is $N_L = 6.025 \times 10^{28}$/m^3. The molar trap concentration was calculated and found to be 0.1174 mol/m^3.

Microstructural analysis

Optical Microscope (Cross section)

The cross section of the samples were observed after the permeation tests.

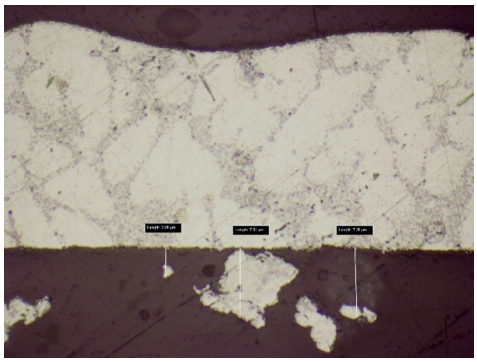

Figure 4.35: Engine Head platinum layer after permeation

In Figure 4.35 the underlying precipitate network within the matrix of the metal which is common for cast alloys. This occurs due to the solidification process during the casting of the alloy wherein Fe and Si are rejected from the growing α-Al dendrites and become concentrated during the final stages of solidification.

Optical Microscopy (Surface)

The Figure 4.36 shows extensive damage to the anode and cathode side of the Engine Head specimen. The anodic surface is heavily fragmented and resembles a "dried earth" pattern. The cathodic side instead has a relatively homogeneous pattern and has a finer texture.

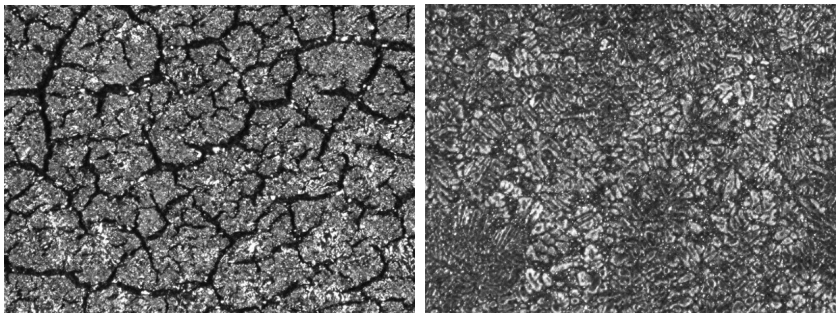

Figure 4.36: a)Left - Anodic side of Engine head after permeation. b) Right – Cathodic side of Engine head after permeation.

SEM-EDS analysis

The surface and the cross section of the cathodic side of the specimen were examined at high magnification using SEM to evaluate the extent of the damage induced by the hydrogen permeation experiment. Figure 4.37 shows damage to the core as well as the surface of the specimen wherein deep pits can be observed near the surface in the cross section.

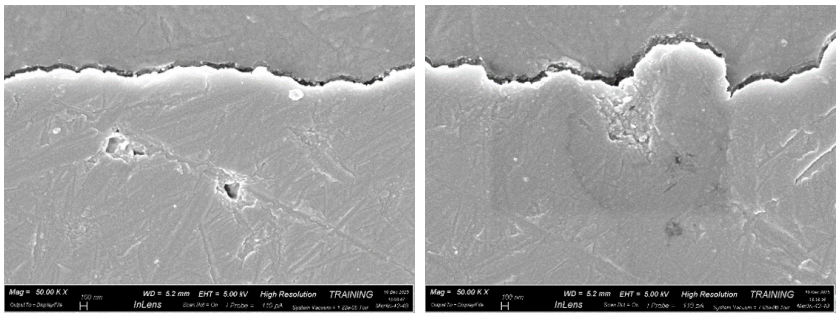

Figure 4.37: Damage caused by permeation to internal structure of Engine Head specimen.

Figure 4.38 shows an interconnected network of intermetallic precipitates throughout the region. Figure 4.38a appears more continuous with bright particulate coverage along the interdendritic boundaries and the cell boundary cracks appear slightly more pronounced and wider. The 4.38b appears to have cracks across the oxide layer in an axis compared to the irregular cracks in Figure 4.38a.

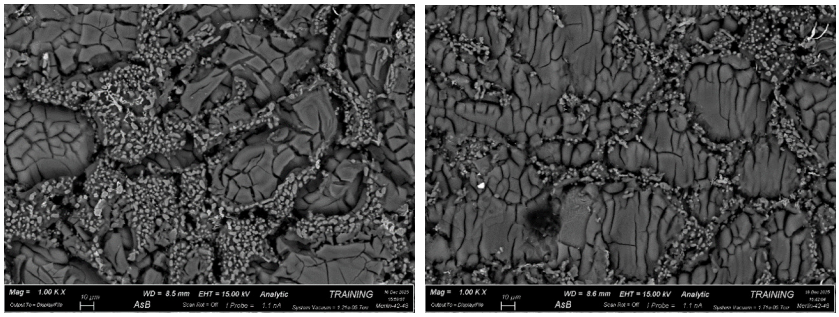

Figure 4.38: Interconnected network of intermetallic precipitates on surface of Engine Head

The specimen was observed under SEM and EDS analysis was performed on the cathodic side of the specimen as it can reveal the segregation of the alloying elements and possible sites associated with hydrogen trapping.
Site 1 was taken at 10 µm scale at 1000× magnification:

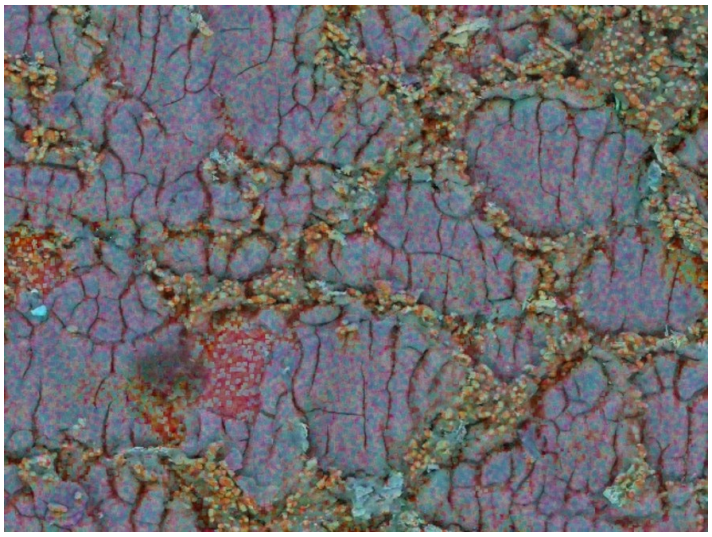

Figure 4.39: Layered EDS elemental map of Site 1 of the Engine Head specimen following hydrogen permeation testing.

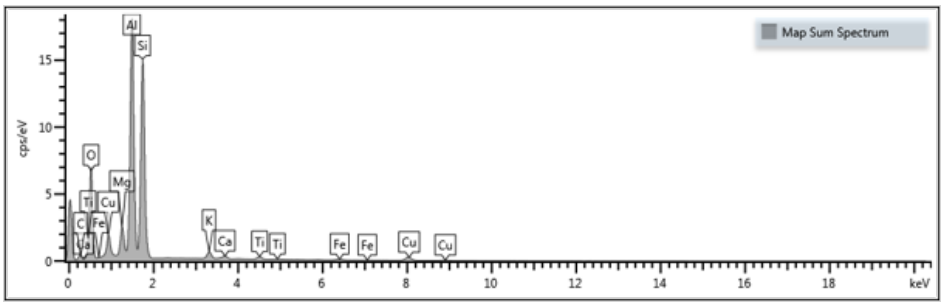

Figure 4.40: EDS map-sum spectrum of the analyzed region after hydrogen permeation testing, showing the characteristic peaks corresponding to aluminium, silicon, and minor alloying elements.

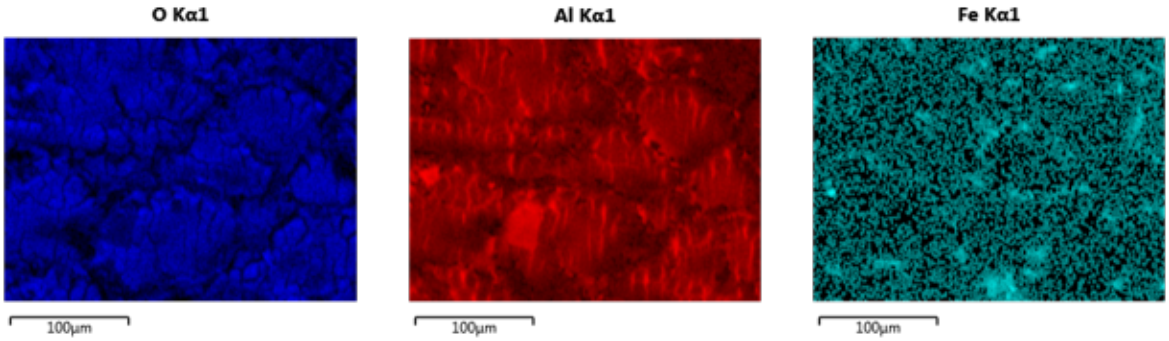

O Kα1 Al Kα1 Fe Kα1

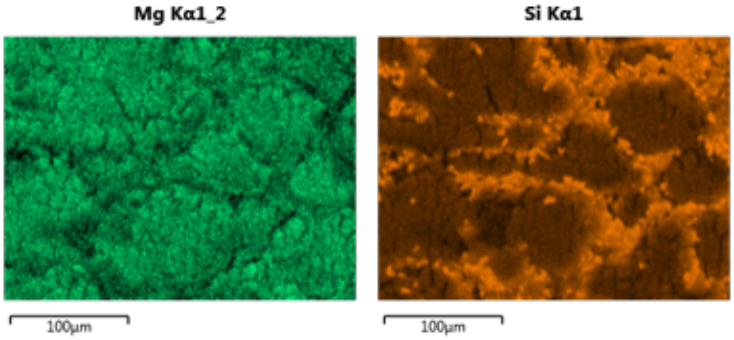

Mg Kα1 Si Kα1

Figure 4.41: EDS elemental maps of the Engine Head alloy after hydrogen permeation testing, showing the distribution of O, Al, K, Fe and Si across the analyzed surface region.

In Figure 4.39, we can observe a continuous network of Silicon Si (orange) which were consistent with the network seen in the Optical Microscope image of the same alloy, specifically in Figures 4.35 and 4.36a.

The Aluminium Al (red) is present in the underlying matrix of the alloy. We can also observe Iron Fe (light blue) in regions surrounding the Si network. Magnesium Mg (dark green) is present uniformly distributed within the matrix. We can gather from Figure 4.44 and Figure 4.35 that the presence of the Fe-Si network provide preferential pathways for hydrogen transport and that results in the abrupt increase in permeation current.

Table 4.12: Quantitative EDS results showing the elemental composition of the analyzed region of the Site 1 of Engine Head alloy after permeation testing.

Element	Atomic %	Weight %
C	10.90	5.99
O	43.59	31.92
Mg	2.80	3.11
Al	19.74	24.39
Si	18.87	24.26
K	0.77	1.38
Ca	0.33	0.60
Ti	0.43	0.94
Fe	0.29	0.75
Cu	2.29	6.66
Total	100.00	100.00

In Table 4.12, the presence of Carbon C (5.99 wt%) is not a constituent of the specimen but could be contamination arising from specimen preparation or residual contaminants present after permeation testing. The relatively high Copper Cu (6.66 wt%) concentration suggests Cu-enriched interdendritic areas within the matrix of the alloy. It also confirms the heterogeneous cast microstructure of the alloy.

Site 2 was taken at 3 µm scale at 3000× magnification:

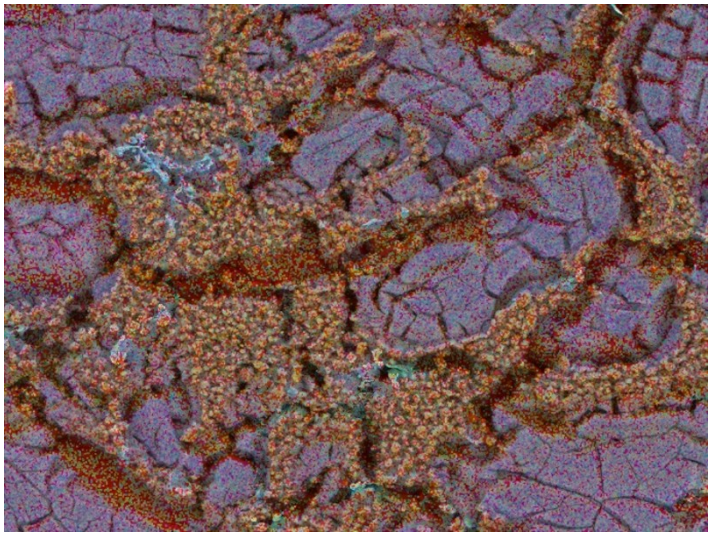

Figure 4.42: Layered EDS elemental map of Site 2 of the Engine Head specimen following hydrogen permeation testing.

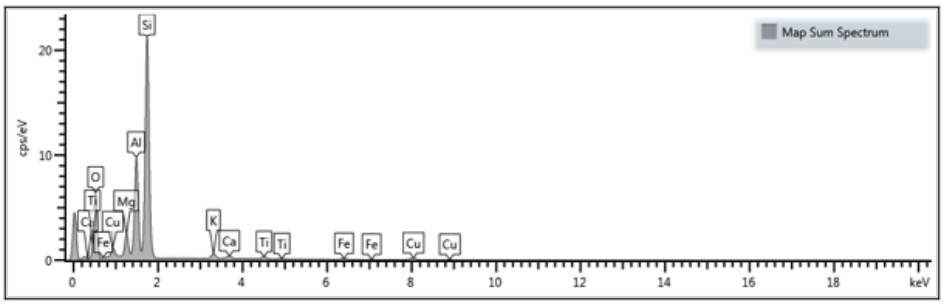

Figure 4.43: EDS map-sum spectrum of the analyzed region after hydrogen permeation testing, showing the characteristic peaks corresponding to silicon as the major elemental composition, and minor alloying elements.

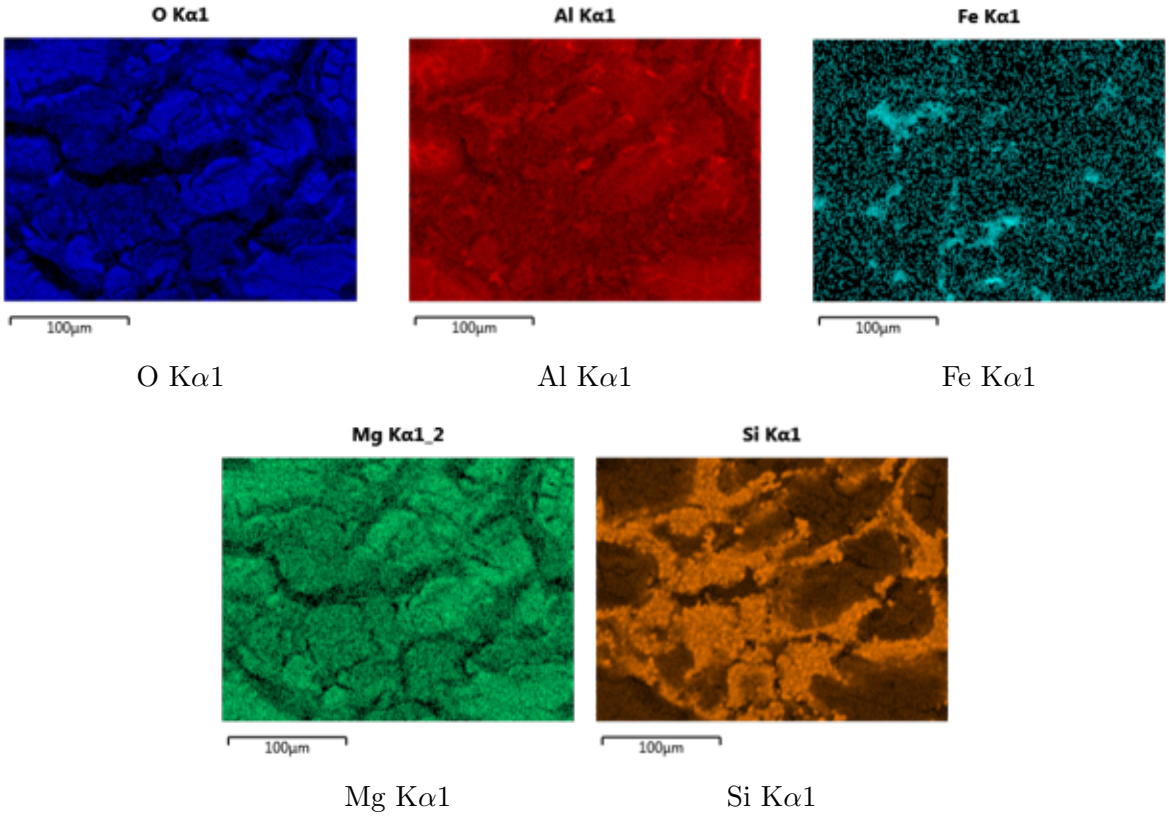

O Kα1 Al Kα1 Fe Kα1

Mg Kα1 Si Kα1

Figure 4.44: EDS elemental maps of the Engine Head alloy after hydrogen permeation testing, showing the distribution of O, Al, K, Fe, Si and Mg across the analyzed surface region.

In Figure 4.42, the EDS elemental maps of site 2 shows that the widespread overlap of Oxygen O (blue) and Aluminium Al (red) distributions suggests the formation of a continuous aluminium oxide layer following hydrogen permeation testing.

Table 4.13: Quantitative EDS results showing the elemental composition of the analyzed region of the Site 2 of Engine Head alloy after permeation testing.

Element	Atomic %	Weight %
O	50.10	35.32
Mg	3.27	3.50
Al	12.66	15.05
Si	30.15	37.31
K	0.85	1.46
Ca	0.47	0.83
Ti	0.54	1.14
Fe	0.43	1.06
Cu	1.54	4.33
Total	100.00	100.00

From the Table 4.13, trace quantities of Calcium Ca (0.83 wt%) and Titanium Ti (1.14 wt%) were detected. The presence of Ca could be a result of contamination or minor impurities, and Ti is commonly added to the alloy as a grain refiner to improve casting properties of the alloy.

Calculation of the volume fraction of precipitates

The thickness of the alloy was measured using Vernier Caliper, the lattice diffusivity and lattice parameter are predetermined values of the metallic properties of Aluminium. The Volume fraction and Mean Area of precipitate was found in Image J analysis of a region of the alloy.
The Mean precipitate radius r in Table 4.15 was measured at 1.184 μ. From this, the interfacial area per unit volume S_v was calculated to be 0.308 $\times 10^5 \mathrm{m}^2/\mathrm{m}^3$. Using the FCC-Al (111) planar atomic density, these stereological measurements yield a geometric trap density N_T^{geo} of 3.17 $\times 10^{23} traps/m^3$.

The calculated geometric trap density is the highest among the investigated alloys, suggesting that A319 possesses the greatest potential for particle-interface trapping. The large number of interfaces increases the probability of hydrogen atoms interacting with microstructural features during diffusion, thereby increasing hydrogen retention within the material. This is consistent with the EDS analysis in Figure 4.39 and 4.42 and the interconnected network of precipitates in Figure 4.38a. The geometric trap density calculation assumes an equivalent spherical particle geometry and therefore does not fully account for the complex morphology of the eutectic Si phase observed in A319. Consequently, the actual influence of the microstructure on hydrogen transport may be greater than that predicted solely from the calculated geometric trap density.

Table 4.14: Microstructural characteristics of A319 (Engine Head) precipitates.

Parameter	Symbol	Value
Specimen thickness	L	6.60×10^{-4} m
Lattice diffusivity	D_L	1.88×10^{-10} m^2/s
Lattice parameter	a	4.049×10^{-10} m
Volume fraction	V_f	12.5 %
Mean precipitate area	$\overline{A}_{\text{precipitate}}$	4.402 μm^2

Table 4.15: Analysis of Geometric Trap density for A319 (Engine Head).

Parameter	Symbol	Value
Mean precipitate radius	r	1.184 μm
Interfacial area per unit volume	S_V	0.308×10^5 m^2/m^3
Geometric trap density	N_T^{geo}	3.17×10^{23} traps/m^3

4.5 A380 (Inlet Manifold)

The inlet manifold that was chosen is also a variant of the Al-4xxx alloy. Chemical characterization of the inlet manifold specimens was performed using optical emission spectroscopy (spark analysis). The composition corresponded to an A380 die-cast aluminium alloy [21] containing approximately 7.5–9.5 wt% Si, 3–4 wt% Cu, 0.1–0.5 wt% Mg, and 1–2 wt% Fe, with aluminium constituting the balance of the alloy.

Permeation tests

The experiment ran for a total of 41.4 hours. Once the current had reached close to 340 µA/cm^2, we add the electrolyte in the cathode compartment. We observed two permeation curves when assessing the current flux as seen in Figure 4.45. The second transient curve was taken to obtain results. The transient current at approximately 315 µA/cm^2 was observed at about 41.2 hours from the start of the experiment.

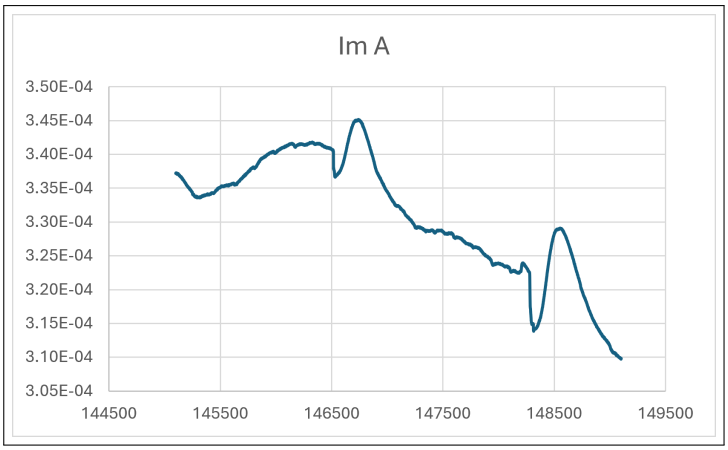

Figure 4.45: Plot showing two transient current curves of A380 (Inlet Manifold) specimen after permeation test.

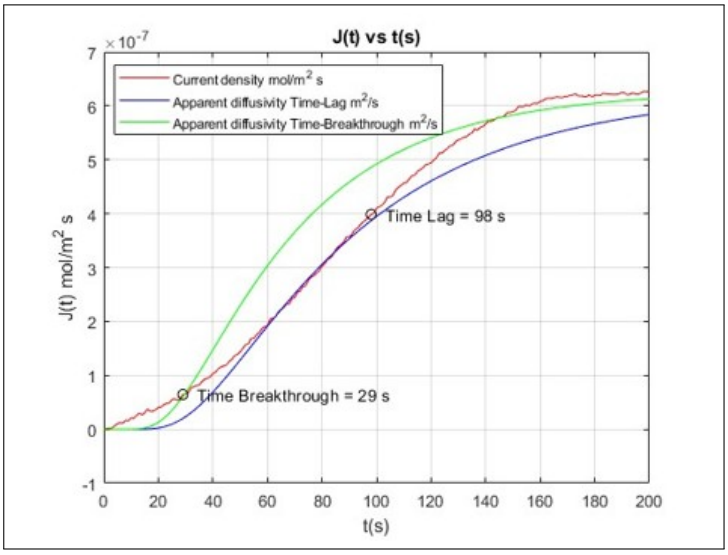

Figure 4.46: Permeation curve of A380 (Inlet Manifold) showing Time Lag and Time Breakthrough

The two permeation curves could indicate surface oxide behaviour or micrstructural heterogeneity within the cast A380 alloy. They were not interpreted as definitive evidence of separate hydrogen diffusion processes. The second transient peak was used for permeation analysis as the initial transient was believed to be influenced by surface and oxide related effects that do not represent the steady hydrogen transport. In Figure 4.46, the transient is extremely quick relative to the short rise time of only 200 seconds given by the Time Lag at 98 seconds which indicates that the hydrogen transport was only minimally delayed by trapping during permeation. The transient current density reaches a stable 6 $\times 10^{-7}$mol/m^{2}s.

From the calculations done on MATLAB, D_{app}^{tl} we obtain a value of 2.72×10^{-10}m^2/s knowing that the lattice diffusivity of hydrogen in Aluminium is $D_L = 1.88 \times 10^{-10}$m^2/s.

The Binding Energy E_b is calculated to be 5.304×10^4J/mol to calculate the number of traps N_T.

We have the calculated number of traps $N_T = -9.38 \times 10^{18}/\text{m}^3$ considering the number of interstitial sites in A380 (Inlet Manifold) is $N_L = 6.025 \times 10^{28}/\text{m}^3$. The molar trap concentration was calculated and found to be $-1.558 \times 10^{-5}\text{mol}/\text{m}^3$.

The number of traps N_T and molar trap concentration C_T being negative indicates that the Oriani's model cannot be applied in this case. The hypotheses that can be drawn is that this alloy has a lot of second phases and therefore hydrogen can go through second phases that have their own diffusivity, which may be greater than that of the aluminium matrix.

Microstructural analysis

Optical Microscope (Cross section)

The cross section of the samples were observed after the permeation tests.

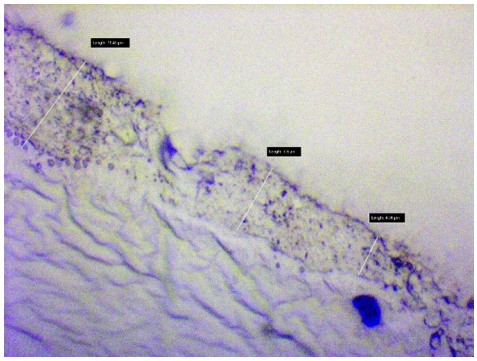

Figure 4.47: Oxide layer formed over Inlet Manifold specimen surface

Figure 4.47 shows the oxidation of Aluminium (black patches) over the surface close to the Platinum layer of the Inlet Manifold specimen.

Optical Microscopy (Surface)

The Figure 4.48 shows a similar level of damage to the surface on both the anodic and cathodic side of the specimen. At first there appears to be no apparent damage due to the hydrogen permeation. This could mean hydrogen takes "short cuts" through the specimen to reach the oxidation (Anodic) side. This is evident with the Apparent Diffusivity (D^{tl}_{app}) being greater than the Lattice Diffusivity D_L.

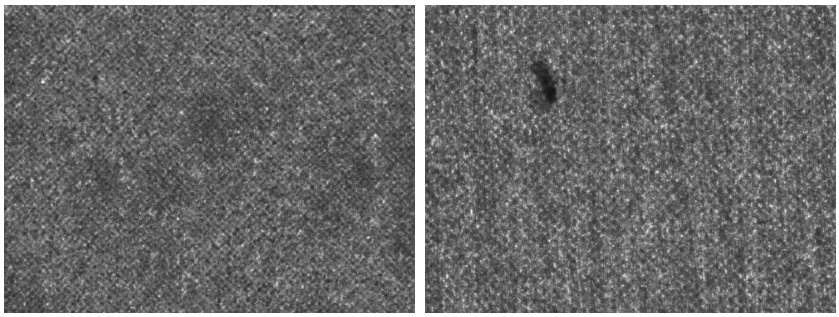

Figure 4.48: a) Left – Anode side of Inlet Manifold after permeation. b) Right – Cathode side of of Inlet Manifold after permeation.

SEM-EDS analysis

In Figure 4.49 damage on the surface of the cathodic side of the specimen. The specimen appears to have numerous white grains on the underlying surface which draws similar comparisons to the Al-6016 Pristine specimen. Above these grains the damage is quite apparent when viewed under SEM.

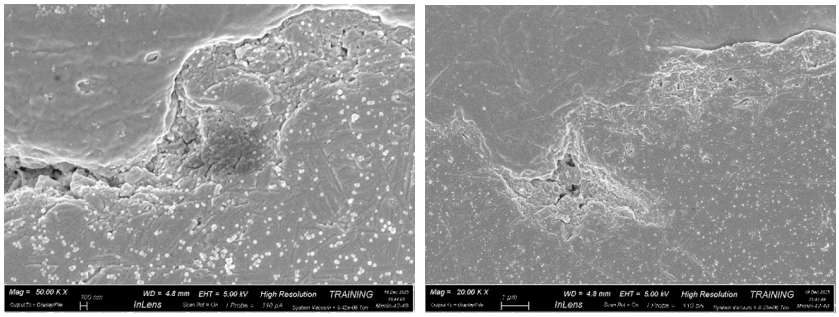

Figure 4.49: Damage caused by permeation to internal structure of Inlet Manifold specimen.

A notable difference between the two automotive specimen is the morphology of the surface features observed in Figure 4.50. It shows the Inlet Manifold specimen contains isolated polygonal particles distributed. These images were used to perform EDS analysis.

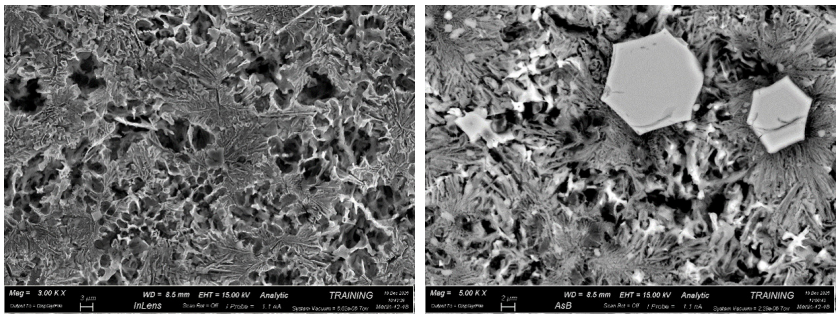

Figure 4.50: SEM micrograph of the inlet manifold alloy after hydrogen permeation testing, showing large polygonal intermetallic particles embedded within a the microstructure.

Site 1 was taken at 3 µm scale at 3000× magnification:

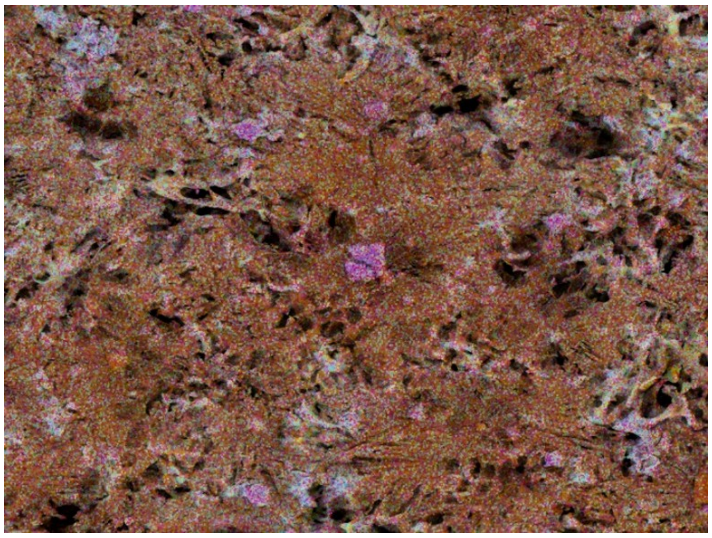

Figure 4.51: Layered EDS elemental map of Site 1 of the Inlet Manifold specimen following hydrogen permeation testing.

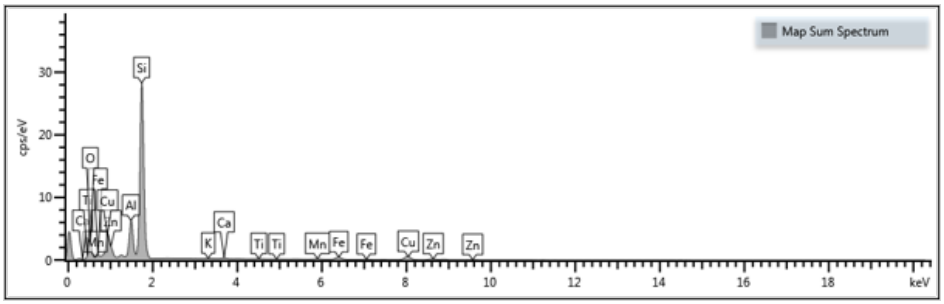

Figure 4.52: EDS map-sum spectrum of the analyzed region after hydrogen permeation testing, showing the characteristic peaks corresponding to silicon as the major elemental composition, and minor alloying elements

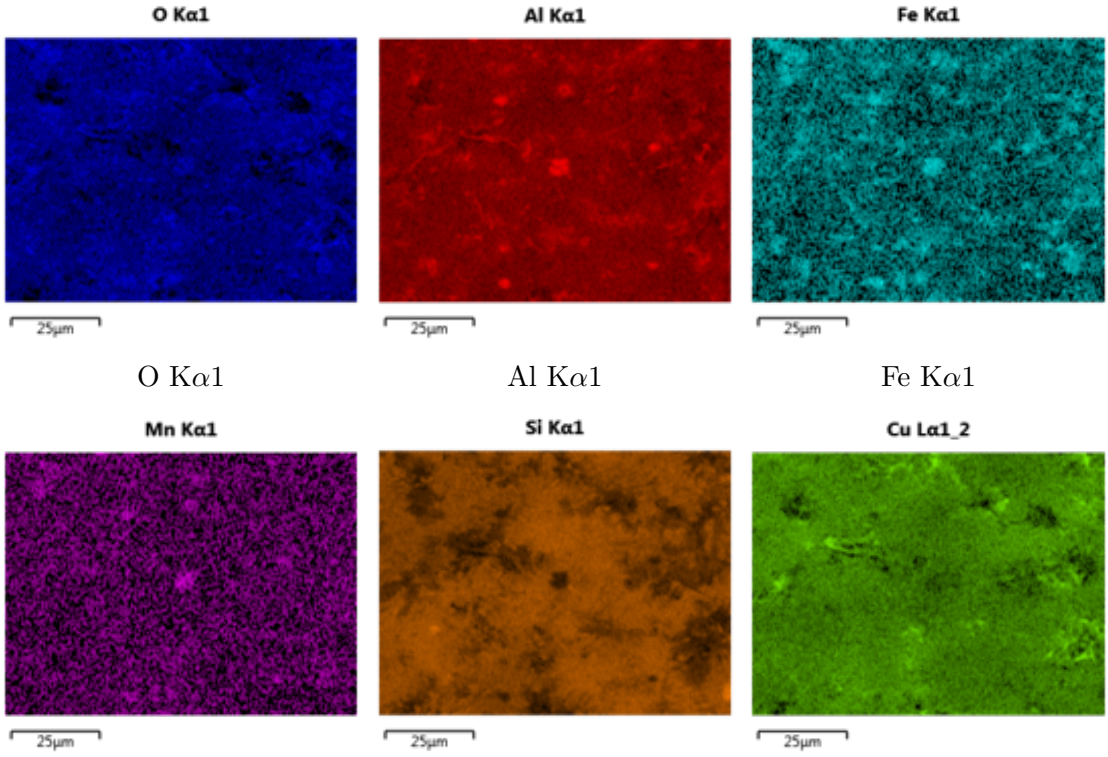

Figure 4.53: EDS elemental maps of the Engine Head alloy after hydrogen permeation testing, showing the distribution of O, Al, K, Fe, Si, Mn and Cu across the analyzed surface region.

In Figure 4.51, we can a large distribution of Copper Cu (green) in parts of the matrix of the alloy. Iron Fe (light blue) and Manganese Mn (magenta) appear to be co-localized in large concentrations, although Mn is only localized in very few regions where the Aluminium Al (red) is largely prevalent.

Table 4.16: Quantitative EDS results showing the elemental composition of the analyzed region of the Site 1 of Inlet Manifold alloy after permeation testing.

Element	Atomic %	Weight %
O	27.51	15.18
Al	10.81	10.06
Si	48.54	47.03
K	0.11	0.15
Ca	0.40	0.56
Ti	0.17	0.27
Mn	0.52	0.98
Fe	2.22	4.28
Cu	6.90	15.12
Zn	2.83	6.38
Total	100.00	100.00

In Table 4.16, Copper Cu (15.12 wt%) is a major alloying element of A380 aluminium alloys and is added to improve strength. The measured Zinc Zn (6.38 wt%) content is higher than that expected for the nominal alloy composition, suggesting local surface enrichment. The presence of these secondary phase elements may influence the transport of hydrogen which might give insight as to why the Oriani's model for this alloy failed.

Site 2 – Taken at 2 µm scale at 5000× magnification:

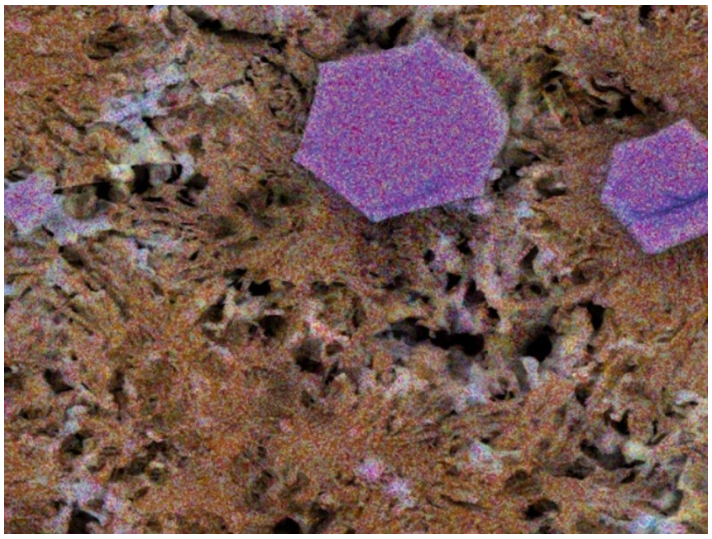

Figure 4.54: Layered EDS elemental map of Site 2 of the Inlet Manifold specimen following hydrogen permeation testing.

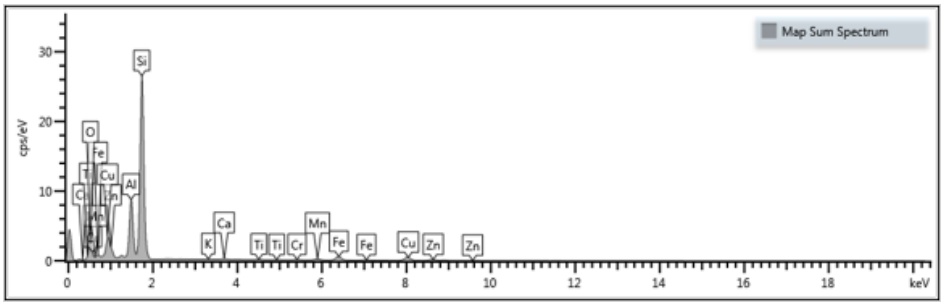

Figure 4.55: EDS map-sum spectrum of the analyzed region after hydrogen permeation testing, showing the characteristic peaks corresponding to silicon as the major elemental composition, and minor alloying elements.

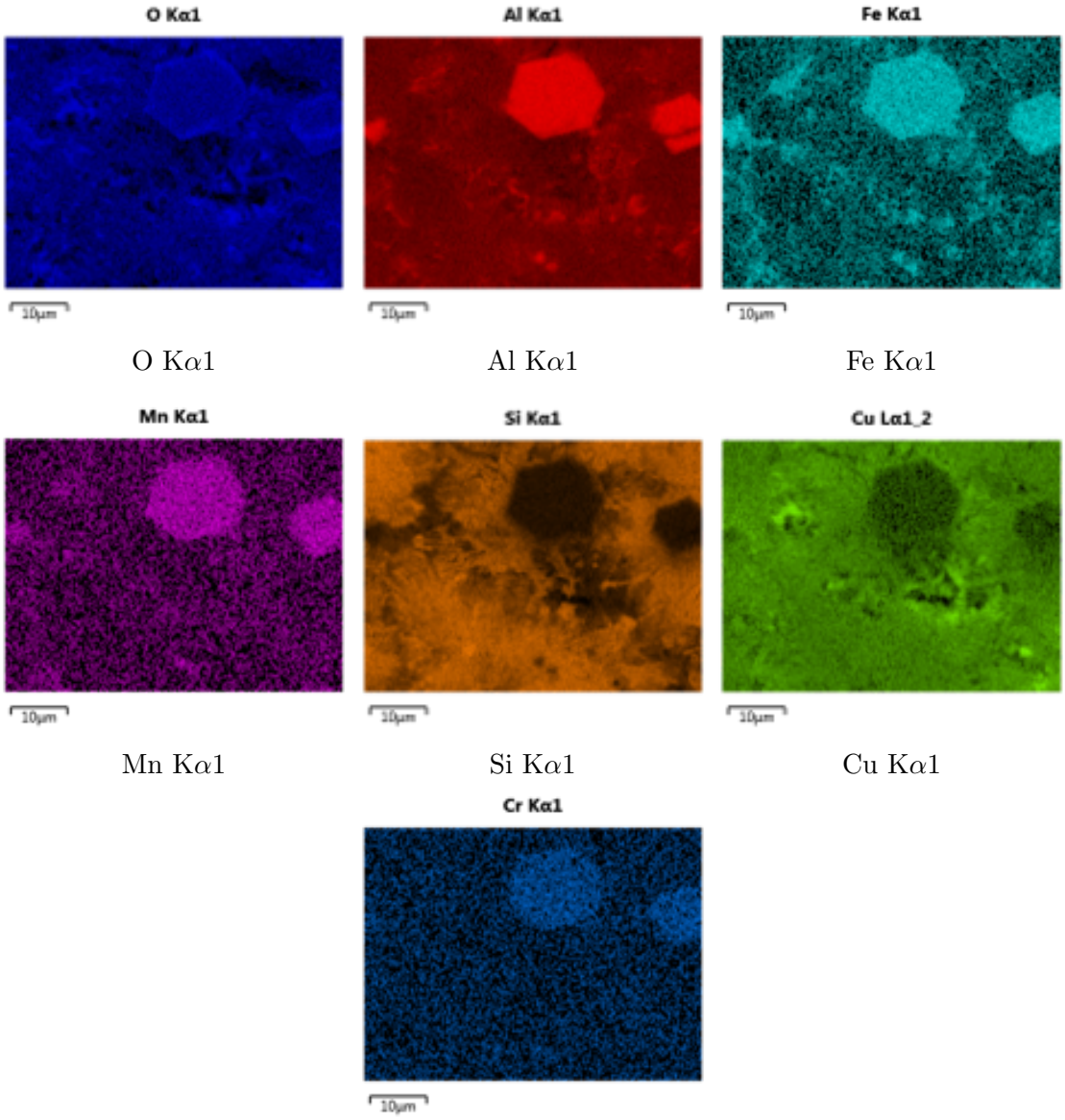

Figure 4.56: EDS elemental maps of the Engine Head alloy after hydrogen permeation testing, showing the distribution of O, Al, K, Fe, Si, Mn, Cr and Cu across the analyzed surface region.

From Figure 4.54, we observed that Aluminium Al (red), Manganese Mn (magenta) and Iron Fe (light blue) and even Chromium Cr (cyan blue) is concentrated mainly in the large hexagonal intermetallic region.

These large hexagonal elements can be considered as the secondary phase precipitates within the alloy, as they harbor many different metals forming a complex intermetallic phase which provides an ideal site for hydrogen trapping.

Table 4.17: Quantitative EDS results showing the elemental composition of the analyzed region of the Site 2 of Inlet Manifold alloy after permeation testing.

Element	Atomic %	Weight %
O	25.85	14.25
Al	14.91	13.86
Si	46.13	44.64
K	0.10	0.14
Ca	0.35	0.48
Ti	0.17	0.28
Cr	0.24	0.42
Mn	0.85	1.60
Fe	3.01	5.79
Cu	5.97	13.06
Zn	2.43	5.48
Total	100.00	100.00

From Table 4.17, the coexistence of Cu (13.06 wt%), Fe (5.79 wt%), Mn (1.60 wt%) and Cr (0.42 wt%) indicates that hydrogen transport occurs through a complex microstructure rather than a single homogeneous aluminium lattice. This microstructural complexity may contribute to the inability of Oriani's trapping model to adequately describe the permeation behaviour observed for the inlet manifold specimen.

Calculation of the volume fraction pf precipitates

The Mean precipitate radius r in Table 4.19 was measured at 0.073 μ. From this, the interfacial area per unit volume S_v was calculated to be 9.74 $\times 10^5 \mathrm{m}^2/\mathrm{m}^3$. Using the FCC-Al (111) planar atomic density, these stereological measurements yield a geometric trap density N_T^{geo} of 9.74 $\times 10^{23} traps/m^3$.

Table 4.18: Microstructural characteristics of A380 (Inlet Manifold) precipitates.

Parameter	Symbol	Value
Specimen thickness	L	4.0×10^{-4} m
Lattice diffusivity	D_L	1.88×10^{-10} m^2/s
Lattice parameter	a	4.049×10^{-10} m
Volume fraction	V_f	23.883 %
Mean precipitate area	$\overline{A}_{\text{precipitate}}$	0.017 μm^2

Table 4.19: Microstructural characteristics of A380 (Inlet Manifold) precipitates.

Parameter	Symbol	Value
Mean precipitate radius	r	0.073 μm
Interfacial area per unit volume	S_V	9.74×10^5 m^2/m^3
Geometric trap density	N_T^{geo}	9.74×10^{23} traps/m^3

The inability to reliably apply Oriani's trapping model to A380 suggests that the assumptions of local equilibrium trapping may not be fully satisfied in this alloy. Given the very high density of particle-interface traps indicated by the geometric analysis, hydrogen transport may be governed predominantly by lattice diffusion or by trapping mechanisms associated with microstructural defects or precipitates not captured by the geometric model. Consequently, the calculated geometric trap density should be interpreted as a measure of available interface area rather than a true density of active Oriani traps.

Chapter 5

Discussion

The hydrogen trapping behaviour varied considerably among the investigated aluminium alloys, reflecting differences in precipitate morphology, interfacial area, and microstructural complexity. For the Al-4015 alloy, a moderate precipitate interfacial area density and geometric trap density were determined. The substantially large difference between the permeation-derived trap density and the geometrically estimated trap density indicates that hydrogen trapping cannot be explained solely by the observed precipitate interfaces and that additional microstructural features may contribute to the experimentally inferred trapping behaviour. Consequently, hydrogen transport in this alloy is only moderately affected by trapping, with diffusion behaviour approaching that of lattice diffusion.

In contrast, the Al-5083 the geometric trap densities are many orders of magnitude larger than the permeation derived values. This indicates poor agreement between the two approaches and suggests that the assumptions used in the Oriani analysis or geometric estimation may not fully capture the trapping behaviour in these alloys. In Al-5083, trapping may be associated with Mg-related defects, grain boundaries and dislocations rather than solely precipitate interfaces. For Al-6016, the discrepancy is particularly large despite the long permeation transient and dense precipitate distribution observed by SEM. However, the active interface fraction exceeds 100%, demonstrating that the measured hydrogen trapping cannot be explained solely by precipitate interfaces. This discrepancy suggests the presence of additional trapping sites, including Mg–vacancy complexes, grain boundaries, and dislocation structures, all of which have previously been identified as effective hydrogen traps in Al–Mg alloys [26]. The combined contribution of these microstructural features substantially increases the overall hydrogen retention capacity of the alloy.

The Al-6016 alloy displayed the highest permeation-derived trap density and active interface fraction, indicating the strongest hydrogen trapping behaviour among all the investigated materials. The significant difference between the geometric trap density and the experimentally determined trap density suggests that hydrogen trapping is not

restricted to precipitate interfaces alone. As for the previous alloy, in addition to Mg_2Si precipitates, grain boundaries, dislocation substructures, and precipitate–matrix interfaces are likely to form an interconnected trapping network that effectively immobilizes hydrogen and significantly reduces its apparent diffusivity.

A markedly different behaviour was observed for one of the as-cast alloys. The Engine Head (EH) specimen contained relatively coarse intermetallic particles, resulting in a substantially lower precipitate interfacial area density than the wrought alloys. This suggests that the extensive eutectic Si network and intermetallic particle interfaces observed by SEM contribute significantly to the trapping behaviour measured during permeation.

In contrast, the Inlet Manifold (IM) exhibited the coarsest precipitate morphology and the lowest precipitate interfacial area density of all the investigated specimens, indicating a sparse distribution of potential precipitate-related trapping sites. We can assume the hydrogen diffusion is likely controlled by the complex cast microstructure, where interconnected interdendritic regions, porosity, microcracks, and other casting defects provide preferential pathways for hydrogen migration, thereby masking the contribution of conventional precipitate-related trapping sites.

In conclusion, across the six specimens, the permeation behaviour and EDS maps converge on two distinct regimes:

- Lattice/trap-controlled diffusion (reference wrought alloys): Al-4015, Al-5083, and Al-6016 all exhibit $D_{app} < D_L$ and physically valid Oriani parameters. The progressive reduction in D_{app} (4015 > 5083 >> 6016) tracks the increasing complexity and strength of the trap landscape visible or inferred from EDS: from sparse Si-interface traps in Al-4015, through grain-boundary and Mg-vacancy dominated trapping in Al-5083, to a combination of Mg_2Si precipitate interfaces, grain boundaries, and dislocation substructures in Al-6016.

- Surface- and defect-barrier-controlled transport (cast engine components): The Engine Head and Inlet Manifold both show $D_{app} > D_L$, invalidating the trapping model. The EDS maps of both specimens reveal coarse Si-rich interdendritic networks, thick oxide layers, and Cu-bearing phases - features associated with die-casting microstructures that facilitate rapid hydrogen transport through surface-barrier release and short-circuit paths (porosity, eutectic channels, microcracks) rather than classical bulk diffusion. These specimens are therefore more susceptible to sudden hydrogen ingress events under operational conditions than their wrought counterparts.

Chapter 6

Conclusion

This thesis investigated hydrogen permeation behaviour across five commercially relevant aluminium alloy specimens – three reference alloys (Al-4015, Al-5083 and Al-6016) and two automotive engine components A319 (Engine head) and A380 (Inlet manifold) - using the electrochemical Devanathan–Stachurski (DS) permeation technique[8].

Several limitations of the present study should be acknowledged. All permeation experiments were conducted at room temperature, whereas engine components in hydrogen internal combustion engines operate across a wide thermal range. As Oriani[12] demonstrated, both trap binding energies and effective diffusivity are temperature-dependent, and elevated temperatures will progressively deactivate reversible trap sites, increase lattice diffusivity, and alter the balance between trapping and permeation rates. Furthermore, the single-charge permeation transients recorded in this study represent equilibrium trapping conditions; the effects of cyclic hydrogen loading were not investigated. The thin die-cast Inlet Manifold specimen (0.30–0.50 mm) presented the greatest experimental challenge, with the double-peak permeation curve suggesting that specimen integrity may have been partially compromised by pre-existing microcracks. Future studies should employ thicker specimens or alternative specimen geometries to decouple bulk diffusion from defect-mediated transport in cast alloys. Additionally, the study was limited to ex-situ microstructural characterization; in-situ hydrogen mapping techniques would allow the direct correlation of hydrogen distribution with specific microstructural features in real time.

In conclusion, this thesis has provided a systematic, quantitative characterisation of hydrogen permeation and trapping across five aluminium alloy specimen representative of the material families used in hydrogen-fuelled automotive engine systems. The results establish a clear ranking, that being the Al-4015 showing near-lattice diffusion, Al-5083 exhibiting moderate trapping and Al-6016 displaying the strongest trapping for the wrought alloys while the Engine Head and Inlet Manifold behave different in their hydrogen transport wherein it is governed primarily by casting-induced microstructural heterogeneities rather than reversible trapping.

These findings demonstrate that hydrogen transport in automotive engine components cannot be assessed solely from alloy composition; the casting microstructure itself plays a critical role in determining hydrogen permeation behaviour. They also address a gap in the literature highlighted by Chen et al.[6], who identified the inadequate understanding of hydrogen-induced degradation in aluminium alloys under automotive hydrogen service conditions as a key safety concern.

As the automotive industry accelerates the adoption of hydrogen internal combustion engines and fuel cell vehicles, the data and mechanistic insights reported here provide a foundation for informed alloy selection, microstructural optimisation, and component design strategies aimed at mitigating hydrogen embrittlement risk in aluminium engine systems.

Bibliography

[1] X. Li, R. Zhao, C. Wan, T. Sui, and X. Ju, "First-principles study on the hydrogen trapping by vacancy and substitutional helium in W–Ta alloy," *Nuclear Materials and Energy*, vol. 36, p. 101460, Sept. 2023.

[2] H. Fujihara, K. Shimizu, H. Toda, A. Takeuchi, and M. Uesugi, "Suppression of Hydrogen Embrittlement due to Local Partitioning of Hydrogen to Dispersed Intermetallic Compound Particles in Al–Zn–Mg–Cu Alloys," *MATERIALS TRANSACTIONS*, vol. 63, no. 10, pp. 1406–1415, 2022.

[3] G. Young and J. Scully, "The diffusion and trapping of hydrogen in high purity aluminum," *Acta Materialia*, vol. 46, pp. 6337–6349, Nov. 1998.

[4] H. Zhao, P. Chakraborty, D. Ponge, T. Hickel, B. Sun, C.-H. Wu, B. Gault, and D. Raabe, "Hydrogen trapping and embrittlement in high-strength Al alloys," *Nature*, vol. 602, pp. 437–441, Feb. 2022.

[5] M. Safyari, N. Khossossi, T. Meisel, P. Dey, T. Prohaska, and M. Moshtaghi, "New insights into hydrogen trapping and embrittlement in high strength aluminum alloys," *Corrosion Science*, vol. 223, Aug. 2023.

[6] Y. Chen, S. Zhao, H. Ma, H. Wang, L. Hua, and S. Fu, "Analysis of Hydrogen Embrittlement on Aluminum Alloys for Vehicle-Mounted Hydrogen Storage Tanks: A Review," *Metals*, vol. 11, p. 1303, Aug. 2021.

[7] R. Walallawita, J. Stroh, and D. Sediako, "The Effect of Hydrogen Embrittlement on Aluminum Alloys Used for Hydrogen-Fueled Internal Combustion Engine," pp. 447–450, Jan. 2023.

[8] M. A. V. Devanathan and Z. Stachurski, "The adsorption and diffusion of electrolytic hydrogen in palladium," *Proceedings of the Royal Society of London. A. Mathematical and Physical Sciences*, vol. 270, pp. 90–102, Oct. 1962.

[9] J. Carvalho, E. Vilar, and B. Araújo, "A critical review and experimental analysis of the equation recommended by ASTM G148-97 and ISO 17081: 2004 for the

calculation of the hydrogen diffusivity in metals and alloys," *International Journal of Hydrogen Energy*, vol. 42, pp. 681–688, Jan. 2017.

[10] A. Zafra, Z. Harris, C. Sun, and E. Martínez-Pañeda, "Comparison of hydrogen diffusivities measured by electrochemical permeation and temperature-programmed desorption in cold-rolled pure iron," *Journal of Natural Gas Science and Engineering*, vol. 98, p. 104365, Feb. 2022.

[11] M. J. Danielson, "Use of the Devanathan–Stachurski cell to measure hydrogen permeation in aluminum alloys," *Corrosion Science*, vol. 44, pp. 829–840, Apr. 2002.

[12] R. Oriani, "The diffusion and trapping of hydrogen in steel," *Acta Metallurgica*, vol. 18, pp. 147–157, Jan. 1970.

[13] R. Shi, L. Chen, Z. Wang, X.-S. Yang, L. Qiao, and X. Pang, "Quantitative investigation on deep hydrogen trapping in tempered martensitic steel," *Journal of Alloys and Compounds*, vol. 854, p. 157218, Feb. 2021.

[14] J. Scully, G. Young, and S. Smith, "Hydrogen Solubility, Diffusion and Trapping in High Purity Aluminum and Selected Al-Base Alloys," *Materials Science Forum*, vol. 331-337, pp. 1583–1600, May 2000.

[15] S. Jiang, Y. Xu, R. Wang, X. Chen, C. Guan, Y. Peng, F. Liu, M. Wang, X. Liu, S. Zhang, G. Tian, S. Jin, H. Wang, H. Toda, X. Jin, G. Liu, B. Gault, and J. Sun, "Structurally complex phase engineering enables hydrogen-tolerant Al alloys," *Nature*, vol. 641, pp. 358–364, May 2025.

[16] Q. Liu, X. Tong, and G. Zhou, "H2O Dissociation-Induced Aluminum Oxide Growth on Oxidized Al(111) Surfaces," *Langmuir*, vol. 31, pp. 13117–13126, Dec. 2015.

[17] P. Natishan and W. O'Grady, "Chloride Ion Interactions with Oxide-Covered Aluminum Leading to Pitting Corrosion: A Review," *Journal of the Electrochemical Society*, vol. 161, pp. C421–C432, June 2014.

[18] G. S. Frankel, "Pitting Corrosion of Metals: A Review of the Critical Factors," *Journal of The Electrochemical Society*, vol. 145, p. 2186, June 1998.

[19] Z. Szklarska-Smialowska, "Pitting corrosion of aluminum," *Corrosion Science*, vol. 41, pp. 1743–1767, Aug. 1999.

[20] e-metal, "Aluminium EN AW-4015 (AlSi2Mn)," 2025.

[21] "Introduction to Aluminum and Aluminum Alloys," in *Metals Handbook Desk Edition* (J. R. Davis, ed.), pp. 417–423, ASM International, 2 ed., Dec. 1998.

[22] USA Department of Defense, *Military Handbook on Aluminum Alloys*. 1966.

[23] V. Kuznetsov, B. Podlovchenko, D. Khanin, V. Zhulikov, and D. Cherkasov, "Preparation of Pd(Mo2C) composites by palladium deposition under open-circuit conditions, their corrosion resistance and catalytic activity," *Journal of Electroanalytical Chemistry*, vol. 979, p. 118913, Feb. 2025.

[24] J. C. Russ and R. T. Dehoff, *Practical Stereology*. Boston, MA: Springer US, 2000.

[25] K. Kim, S.-R. Choi, and J.-G. Kim, "Theoretical and Experimental Study of the Crystal Orientation Effect of the Anode on the Aluminum-Air Battery Performance," *Journal of The Electrochemical Society*, vol. 169, Jan. 2023.

[26] N. Kamel, "Effect of Mg Contents on Trapping Efficiency in Al-Mg System Using PAS," *Defect and Diffusion Forum*, vol. 265, pp. 7–11, May 2007.